Acta Materialia 257 (2023) 119183

Contents lists available at ScienceDirect

Acta Materialia

journal homepage: www.elsevier.com/locate/actamat

Full length article

Chromium-based bcc-superalloys strengthened by iron supplements

Kan Ma [a], Thomas Blackburn [a], Johan P. Magnussen [a], Michael Kerbstadt [b], Pedro A. Ferreirós [a,c], Tatu Pinomaa [c], Christina Hofer [d], David G. Hopkinson [e], Sarah J. Day [e], Paul A.J. Bagot [d], Michael P. Moody [d], Mathias C. Galetz [b], Alexander J. Knowles [a,*]

[a] School of Metallurgy and Materials, University of Birmingham, Birmingham B15 2TT, United Kingdom
[b] DECHEMA-Forschungsinstitut, High Temperature Materials, Theodor-Heuss-Allee 25, 60486, Frankfurt am Main, Germany
[c] VTT Technical Research Centre of Finland Ltd, 02150, Espoo, Finland
[d] Department of Materials, University of Oxford, Parks Road, Oxford, OX1 3PH, United Kingdom
[e] Diamond Light Source Ltd, Harwell Science and Innovation Campus, Didcot, Oxfordshire, OX11 0DE, United Kingdom

ARTICLE INFO

Keywords:
Chromium
Bcc-superalloy
Coarsening kinetics
Strengthening
Electron microscopy

ABSTRACT

Chromium alloys are being considered for next-generation concentrated solar power applications operating > 800 °C. Cr offers advantages in melting point, cost, and oxidation resistance. However, improvements in mechanical performance are needed. Here, Cr-based body-centred-cubic (bcc) alloys of the type Cr(Fe)-NiAl are investigated, leading to 'bcc-superalloys' comprising a bcc-Cr(Fe) matrix (β) strengthened by ordered-bcc NiAl intermetallic precipitates (β'), with iron additions to tailor the precipitate volume fraction and mechanical properties at high temperatures. Computational design using CALculation of PHAse Diagram (CALPHAD) predicts that Fe increases the solubility of Ni and Al, increasing precipitate volume fraction, which is validated experimentally. Nano-scale, highly-coherent B2-NiAl precipitates with lattice misfit ~ 0.1% are formed in the Cr (Fe) matrix. The Cr(Fe)-NiAl A2-B2 alloys show remarkably low coarsening rate (~10^2 nm^3/h at 1000 °C), outperforming ferritic-superalloys, cobalt- and nickel-based superalloys. Low interfacial energies of ~ 40/20 mJ/m^2 at 1000/1200 °C are determined based on the coarsening kinetics. The low coarsening rates are principally attributed to the low solubility of Ni and Al in the Cr matrix. The alloys show high compressive yield strength of ~320 MPa at 1000 °C. The Fe-modified alloy exhibits resistance to age softening, related to the low coarsening rate as well as the relatively stable Orowan strengthening as a function of precipitate radius. Microstructure tailoring with Fe additions offers a new design route to improve the balance of properties in "Cr-superalloys", accelerating their development as a new class of high-temperature materials.

1. Introduction

As an important part of low-carbon energy deployment, next-generation concentrated solar plants (CSP), operating between 700 and 1000 °C, aim to integrate ceramic particles as the primary heat transfer medium allowing thermal energy storage, with a secondary loop of supercritical carbon dioxide (s-CO_2) utilising Brayton power cycles to improve thermal efficiency [1–6]. However, this design creates significant material challenges for the heat exchanger tubes, including strength, creep, erosion/wear resistance at temperatures T > 700 °C, alongside resistance to oxidation and s-CO_2 corrosion [2,3]. While some advanced austenitic stainless steels and nickel-based superalloys provide an acceptable balance of properties at T = 600–800 °C, a further increase in service temperature is limited by their strength/corrosion at T > 800 °C [7,8]. Thus, the development of high-performance alloys based on refractory metals are sought for advanced CSP applications.

Chromium (Cr) based materials are considered attractive for high-temperature applications, initially for jet engines [9] and nowadays for CSP [5], due to their high melting point (1907 °C for Cr, compared with nickel (Ni) (1455 °C) and iron (Fe) (1538 °C) [10]), low cost (compared to Ni and other refractory metals, see Section S1), low density, good thermal conductivity, and exceptional oxidation resistance [11], *cf.* Table S1. Since the first consideration of a Cr base alloy system in the 1940s, it is known that the strengthening and ductilisation of Cr alloys is a key point for the deployment of their application [12]. During the 1950s and 60s, extensive research was conducted into binary additions to Cr. While it is mostly accepted that pure Cr is brittle at room temperature, the ductility of pure Cr is still debatable as its ductile to

* Corresponding author at: School of Metallurgy and Materials, University of Birmingham, Birmingham, B15 2TT.
E-mail address: A.J.Knowles@bham.ac.uk (A.J. Knowles).

https://doi.org/10.1016/j.actamat.2023.119183
Received 12 May 2023; Received in revised form 21 July 2023; Accepted 22 July 2023
Available online 26 July 2023

brittle transition temperature (DBTT) varied from −196 °C to 300 °C, which was reported to depend strongly on its purity, particularly on the nitrogen content [13]. It was found that the DBTT of Cr is also sensitive to the grain structure and surface conditions [14–16]. Furthermore, solute additions tend to strengthen Cr as well as ductilising it. But the effect of solute addition is complex. Some elements may lower the hardness of Cr at low concentrations, referring to solution softening effects [17,18]. Rhenium and some other elements (*e.g.* Fe) showed ductilising effects [19–21]. However, with a gap of research on Cr alloys appearing since the 1980s, chromium-based alloys for high-temperature uses still face challenges in high-temperature strength, room temperature ductility and oxidation resistance above 900 °C [22].

Inspired by the $\gamma - \gamma'$ microstructure of face-centred cubic (fcc) Ni-based superalloys, which exhibit an exceptional combination of strength, oxidation resistance and toughness [23], a new look to the design of Cr alloys has been taken. A "bcc-superalloy" design strategy has been recently proposed in many body-centred cubic (bcc) metals, *e.g.* Fe [24,25], Cr [26–28], tungsten (W) [29], titanium (Ti) [30] to create alloys with high strength. These alloys comprise a A2-type[1] disordered bcc matrix (so-called β phase) with ordered-bcc intermetallic precipitates (so-called β' phase), such as B2-type[1] (CsCl structure) NiAl or TiFe, and $L2_1$-type[1] $AlNi_2Ti$. Cr-NiAl alloys follow the bcc-superalloy strategy and are analogous to the well-developed Fe-NiAl ferritic superalloys, but Cr-NiAl remains a nascent class of materials with only limited data to date. It has been reported that highly coherent B2-NiAl precipitates adopting a cube-cube orientational relationship can be finely dispersed in the A2-Cr matrix after thermal ageing [26,27]. The theoretical lattice misfit (δ) is low and is expected to be $|\delta| = <0.1\%$ at room temperature (a_{Cr} = 288.5 pm [31] and a_{NiAl} = 288.7 pm [32]), although the misfit has not yet been experimentally determined. This design is expected to strengthen the alloys with improved creep resistance without degrading the existing ductility. Creep experiments showed that the presence of the NiAl phase significantly improves the creep resistance of Cr compared to unreinforced Cr at 850 °C [28]. These alloys are referred to as Cr-based "bcc-superalloys" ("Cr-superalloy" for short) as similarly defined for other novel alloys utilising a $\beta - \beta'$ "bcc-superalloys" microstructure concept, for example, ferritic superalloys [33,34], tungsten bcc-superalloys [29], and increasingly commonly now for refractory high entropy superalloys (RSAs) [35–37].

However, unlike Fe-NiAl or Ni-Ni_3Al systems, Cr-NiAl has a large dual-phase (A2-B2) miscibility gap with a narrow A2 single-phase area. It has been proven to be difficult to homogenise the microstructure by heat treatment in Cr-NiAl alloys, with the retention of a dendritic microstructure and primary eutectic NiAl precipitates after homogenisation [28]. Phase diagram calculations (which underpin modern Integrated Computational Materials Engineering (ICME) alloy development) show large discrepancies in the single-phase A2 region between different databases [38–40]. A Cr-NiAl pseudo-binary diagram assessment suggests a maximum solubility limit of about 10%Ni+10%Al (atomic percent, at.%) in the A2-Cr [40], larger than experimental values reported, upon which the majority of CALculation of PHase Diagram (CALPHAD) assessments are currently based [41,42]. Whilst the Cr-Ni-Al ternary system has been quite extensively explored by experiments and simulations, major efforts have been made on the Ni-rich side, leaving critical discrepancies in the predicted A2-Cr(Ni,Al) solubility limit: a key parameter controlling precipitate volume fraction of NiAl precipitates and ageing temperatures. There is a need for new design strategies and improved experimental understanding of A2-Cr(Ni,Al) to enhance the accuracy of CALPHAD models, thus enabling the application of ICME methods to accelerate Cr-superalloy development.

In addition to the investigation of the ternary system, this work presents the first attempt to develop quaternary Cr-superalloys Cr(Fe)-NiAl tailored by Fe additions. Fe is chosen due to its (i) low cost, (ii) large solubility in Cr, (iii) beneficial effect on Ni and Al solubility, and (iv) beneficial effect on strength and ductility [12,20]. The influence of Fe on the microstructure after homogenisation heat treatment is studied. Then, the focus shifts to the ageing behaviour of a quaternary alloy and its corresponding ternary system, compared to the ferritic, nickel and cobalt superalloys. The mechanical properties including age softening and stress-strain response at room/high temperatures are investigated, followed by detailed microstructure characterisation to understand the thermal stability of β-β' microstructure and deformation mechanisms.

Table 1
Composition (at.%) measured by SEM/EDS.

Nominal (at.%)	Measured composition			
	Cr	Ni	Al	Fe
Cr-3.5Ni-3.5Al	93.2 ± 0.5	3.5 ± 0.3	3.3 ± 0.3	/
Cr-5Ni-5Al	89.7 ± 0.5	5.5 ± 0.3	4.8 ± 0.3	/
Cr-10Ni-10Al	79.9 ± 0.2	10.7 ± 0.3	9.4 ± 0.4	/
Cr-20Ni-20Al	60.0 ± 0.2	19.6 ± 0.2	20.4 ± 0.2	/
Cr-5Ni-5Al-10Fe	80.8 ± 0.1	4.6 ± 0.1	5.1 ± 0.1	9.5 ± 0.1
Cr-10Ni-10Al-20Fe	59.4 ± 0.3	9.8 ± 0.2	10.6 ± 0.1	20.3 ± 0.1

2. Methods

2.1. Preparation of materials

The alloy designs were guided by CALPHAD analysis in the Thermocalc software using the TCHEA-6 database. Four Cr-Ni-Al ternary and two Cr-Ni-Al-Fe quaternary alloys (compositions in Table 1) were prepared by arc melting of pure elemental Cr (>99.995%), Ni (>99.98%), Al (>99.9%), and Fe (>99.98%) under an argon atmosphere, following vacuum cycling. Ti was first melted three times to absorb any remaining oxygen. Then the ingots were melted, turned and remelted four times, cut and broken into pieces and remelted four more times to ensure chemical homogeneity. The bulk composition was measured (Table 1) using a scanning electron microscope (SEM) JEOL-7000F (20 kV) equipped with energy dispersive X-ray spectroscopy (EDS) by averaging five 100×100 μm^2 areas at different positions. Minor casting pores were observed but the area fraction was small (<1%).

The as-cast alloys (about 10×10×5 mm^3) were encapsulated in silica glass ampoules (inner diameter 15 mm and outer diameter 18 mm), with vacuum-argon cycles three times, then backfilled with a partial pressure of argon allowing 1 bar pressure at the heat treatment temperature. Afterwards, the ampoule was heat treated at 1400 °C for 20 h then water quenched to room temperature, intending to homogenise the microstructure. The homogenisation temperature was chosen based on the differential thermal analysis in [26]. To quench the sample after heat treatment, the glass ampoule with the samples inside were removed from the furnace and quenched immediately (~1 s later) into water at room temperature (15–25 °C). The ampoule was then cracked open within the water. The opened ampoule with the samples was stirred inside in water to accelerate the cooling. It was not possible to measure the cooling rate as it is difficult to monitor the temperature of the sample when it is under water. But the sample were in general completely cooled down at most within 20 s from 1400 °C to room temperature. Thus, we would suggest an average cooling rate of > 70 °C/s. To study the ageing behaviour, two homogenised alloys (Cr-5Ni-5Al and Cr-5Ni-5Al-10Fe, atomic percent, used thereafter) were cut into small pieces and encapsulated in the same manner as for the homogenisation treatment, then aged at 1000 °C or 1200 °C for 4/20/100/240 h.

2.2. Microstructural and elemental characterisation

X-ray diffraction (XRD) was performed on powder produced from the Cr-5Ni-5Al and Cr-5Ni-5Al-10Fe alloys aged at 1000 °C (20 h). The

[1] Strukturbericht notation

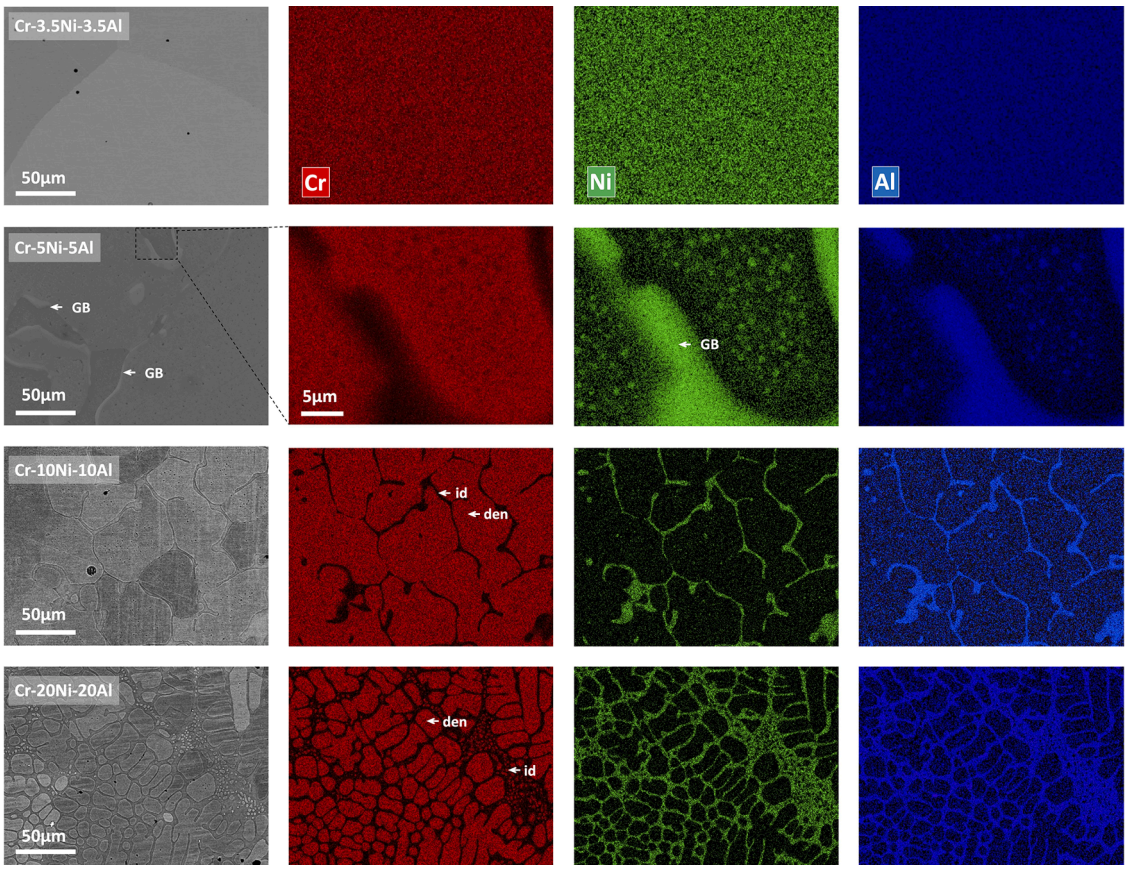

Fig. 1. SEM/EDS showing the microstructure in Cr-3.5Ni-3.5Al, Cr-5Ni-5Al, Cr-10Ni-10Al and Cr-20Ni-20Al after the homogenisation heat treatment at 1400 °C for 20 hr. Dendritic (den) regions are A2-Cr(Ni,Al), secondary phase at grain boundary (GB) and interdendritic (id) regions are B2-NiAl.

powder was obtained by mechanical grinding of the bulk samples, annealed at 500 °C for 15 min under argon to stress relief the powder and then loaded in 0.5 mm diameter borosilicate capillaries. Additional control measurements were made on the grinding powder without the annealing, to ensure that the A2 and B2 peak diffractions were already present and that the low extra oxide peaks observed after the annealing were absent. Synchrotron X-ray diffraction (SXRD) was performed on Beamline I11 at Diamond Light Source using a wide-angle position sensitive detector with an intrinsic 2θ step size of 4 millidegrees; wavelength $\lambda = 82.6596(10)$ pm (calibrated using a NIST Si 640c standard); and a collection time of 120 s. Rietveld refinement of the XRD spectra was performed using FULLPROF Suite to determine the lattice parameters of the Cr(Fe) matrix a_{Cr} and NiAl precipitates a_{NiAl}. The lattice misfit δ between the A2 matrix and B2 precipitates was calculated as [43,44]:

$$\delta = \frac{2(a_{B2} - a_{A2})}{a_{B2} + a_{A2}} \tag{1}$$

SEM samples were ground to a 4000-grit (SiC) surface finish and polished by a colloidal silica polishing suspension. Analysis of the area fraction of different phases and precipitate radius based on SEM images was conducted using the Trainable Weka Segmentation (TWS) plugin in Fiji software [45]. In brief, the TWS plugin was trained to produce a classifier segmenting images into areas of matrix and precipitate phases and applied to the whole image to automatically produce a probability map with homogeneous contrast in both phases, which allows us to distinguish the two-phase areas simply with contrast threshold. Images with complex contrast were also measured using a deep-learning scheme developed recently [46]. Note that the particle radius measured on the plane section based on the SEM image analysis is divided by a factor of 0.82 to convert to 3D precipitate radius [47,48], which is shown on the figures. The probability density P is determined using the following equation [24]:

$$P = \frac{N_i(r, r+\Delta r)}{\sum N_i(r, r+\Delta r)} \frac{\bar{r}}{\Delta r} \tag{2}$$

with $N_i(r,r+\Delta r)$, the number of particles in a given radius interval Δr; $\bar{r}$, the mean radii of precipitates. Standard deviations of precipitate radius are indicated by error bars in the reported size distribution.

Transmission electron microscope (TEM) lamella and atom probe specimens were lifted out using focused ion beam (FIB) equipped on an FEI Quanta 3D field emission gun (FEG) dual-beam SEM. Prior to lamella lift-out, electron backscattering diffraction (EBSD) was performed. Based on the orientation from EBSD, lamellas were lifted out so that their normal were close to a ⟨011⟩ direction to facilitate high-resolution observations. The lamella was successively thinned using 30 keV Ga^+ with a beam current of 1 nA, 0.5 nA, 0.1 nA and 50 pA. After the final step, the lamella was polished until it was transparent at 5 keV electron followed by a cleaning using 5 keV Ga^+ of 48 pA for 2 min. TEM and scanning TEM (STEM)/EDS was performed using a Tecnai F20 at 200 kV equipped with Oxford INCA EDS instrument. The matrix composition in Cr-5Ni-5Al aged at 1200 °C was measured by averaging ten points in the matrix using STEM/EDS. The precipitate composition was measured by averaging ten precipitates larger than 200 nm in diameter to avoid overlap and partial measurement of the surrounding matrix. Aberration-corrected scanning transmission electron microscopy (ac-STEM) using a JEOL ARM300CF microscope operated at 300 kV was used for high-resolution imaging. Angular dark-field (ADF) STEM images were obtained using a probe convergence angle of ~33.6 mrad and an annular detector with an inner and outer radius of ~77 and ~209 mrad, respectively. Background filtering of atomic resolution annular dark-

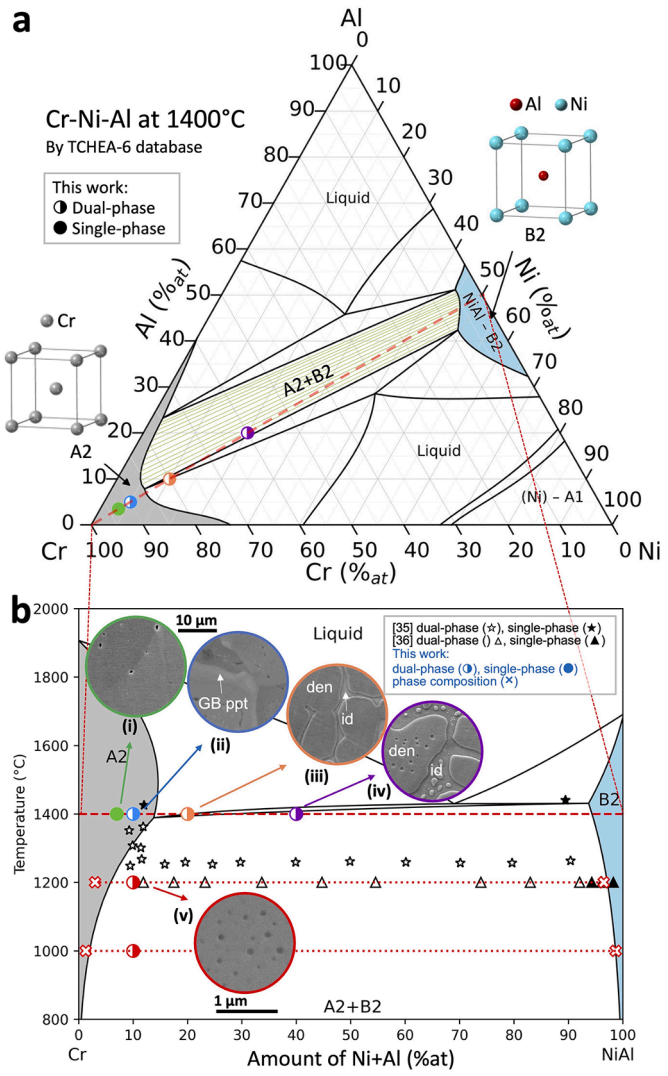

Fig. 2. (a) Ternary phase diagram of Cr-Ni-Al at 1400 °C. (b) Vertical section of equimolar Ni-Al showing the Cr-NiAl binary phase diagram, including data from [41,42] and the present work. Inset SEM micrographs of (i) Cr-3.5Ni-3.5Al, (ii) Cr-5Ni-5Al, (iii) Cr-10Ni-10Al and (iv) Cr-20Ni-20Al after homogenisation at 1400 °C for 20 h showing grain boundary precipitates (GB ppts), dendrites (den) and interdendritic phase (id); microstructure in Cr-5Ni-5Al aged at (v) 1000 °C showing precipitates (ppt).

field STEM images was performed via a radial difference filter (HREM-Filters-v.2.5.1, HREM Research Inc.), matched to the image information limit with edge smoothing of 20%. A 5th order Butterworth filter was applied to FFTs ("Streak-Free FFT", dmscripting.com) to remove streaks due to image edges.

Atom probe tomography (APT) was performed using a Cameca LEAP 5000 XR at the University of Oxford. In APT, samples were analysed using voltage pulsing at a specimen temperature of 50 K, pulse fraction of 20%, pulse frequency of 250 kHz and detection rate of 0.5%. Data reconstruction and analysis were carried out using Cameca AP Suite 6.1 software. The reconstruction was conducted based on the voltage evolution with an image compression factor of 1.65 and a k factor of 3.3. The initial tip radius was adjusted to obtain spherical precipitates as observed in SEM and TEM. The peak at 29 Da was assigned to Ni^{2+}. The peak at 27 Da was assigned to Cr^{2+} within the matrix and Fe^{2+} within the precipitates according to the natural abundance of the isotopes. The composition of the matrix was obtained from an atom-count weighted average of five regions of interest and the composition of the precipitates was determined inside 40at.%Ni isoconcentration surfaces.

2.3. Mechanical properties

Compression tests were performed on 4 mm diameter cylinders of 6 mm length with a strain rate of $3.3 \times 10^{-4} s^{-1} (\sim 2 \mu m s^{-1})$ at 25/300/450/800/900/1000 °C in air using an Inspekt 50 compression rig. Cylinders were sectioned using electrical discharge machining (EDM) followed by surface grinding using P500 SiC paper. A thermocouple (uncertainty of ±10 °C) was placed close to the sample during the compression to monitor the temperature. Vickers hardness was measured using 0.5 kg load. The spacing of the indentation is 500 µm, about 10 times larger than the indents, repeated in least five different places across the sample. The spacing of indentation is large enough to avoid the effect from each other and to measure different grains. Standard deviations are indicated by error bars in the reported average hardness. A binary alloy Cr-10at.%Fe was arc melted, and homogenised at 1400 °C for 20 h. The hardness of the Cr-10Fe alloy was measured and approximated as the hardness of the matrix phase of Cr-5Ni-5Al-10Fe for the analysis of strengthening mechanisms.

3. Results

3.1. Alloy design and phase diagram of the Cr-Ni-Al system

The Cr-superalloys studied are designed to comprise finely dispersed B2-NiAl precipitates in an A2-Cr matrix. A key point in alloy design is to select alloys with a single phase A2 field at high temperatures and a dual phase A2+B2 at intermediate temperatures, allowing a two-step thermal process of A2 homogenisation and B2 precipitation. The limit of the amount of solutes, namely solubility, is important as it determines the precipitate volume fraction and the strengthening effects. The microstructure of the four ternary alloys after the heat treatment at 1400 °C for 20 h are shown in Fig. 1. The homogenisation is not achieved in Cr-20Ni-20Al, Cr-10Ni-10Al and Cr-5Ni-5Al. Dendritic microstructures are observed in Cr-20Ni-20Al and Cr-10Ni-10Al alloys. The dendrite phase is rich in Cr and surrounded by a continuous interdendritic phase, identified as NiAl, based on SEM-EDS characterisation. The microstructure of Cr-5Ni-5Al is not dendritic but shows a secondary B2 phase at grain boundaries (GB). A single-phase microstructure is successfully achieved for Cr-3.5Ni-3.5Al, avoiding the formation of eutectic or GB precipitates. The area fraction of the micron-scale interdendritic NiAl phase is 4% for Cr-5Ni-5Al, 13% for Cr-10Ni-10Al, and 35% for Cr-20Ni-20Al.

The ternary phase diagram of Cr-Ni-Al at 1400 °C is plotted in Fig. 2 (a). The Cr-Ni-Al ternary system has a wide A2+B2 field, with indeed a potential for single-phase A2 alloys solution heat-treated at 1400 °C and B2 precipitation at lower temperatures. The compositions and microstructure types (single-phase or dual-phase) of the studied ternary alloys after homogenisation heat treatment at 1400 °C are plotted in the ternary phase diagram in Fig. 2(a). The measured compositions are close to the nominal values as can be seen in Fig. S1 in Supplementary Materials. For simplicity, nominal compositions are plotted in the equiatomic vertical section in Fig. 2(b). The maximum solubility of Ni and Al within the single-phase A2 Cr matrix at 1400 °C is found to be significantly overestimated by CALPHAD when compared to the experimental findings. It is worth mentioning that, in all four alloys, fine secondary NiAl precipitates are observed in the matrix; these are likely to form during cooling after homogenisation due to the low nucleation barrier in A2-B2 systems [49].

Nano-scale spherical B2-NiAl precipitates are observed in both 1200 °C and 1000 °C heat-treatment conditions. To further assess the A2 to B2 solvus, the compositions of both phases were measured in the Cr-5Ni-5Al alloy after ageing at 1200 °C for 20 h, giving 97.8Cr-1.3Ni-0.9Al (A2) and 4.8Cr-52.7Ni-42.5Al (B2) by STEM/EDS. Most of precipitates have a diameter larger than the sample thickness which allows for avoiding the signal contribution from the matrix. For the sample aged at 1000 °C for 20 h, the precipitates are small so the compositions were

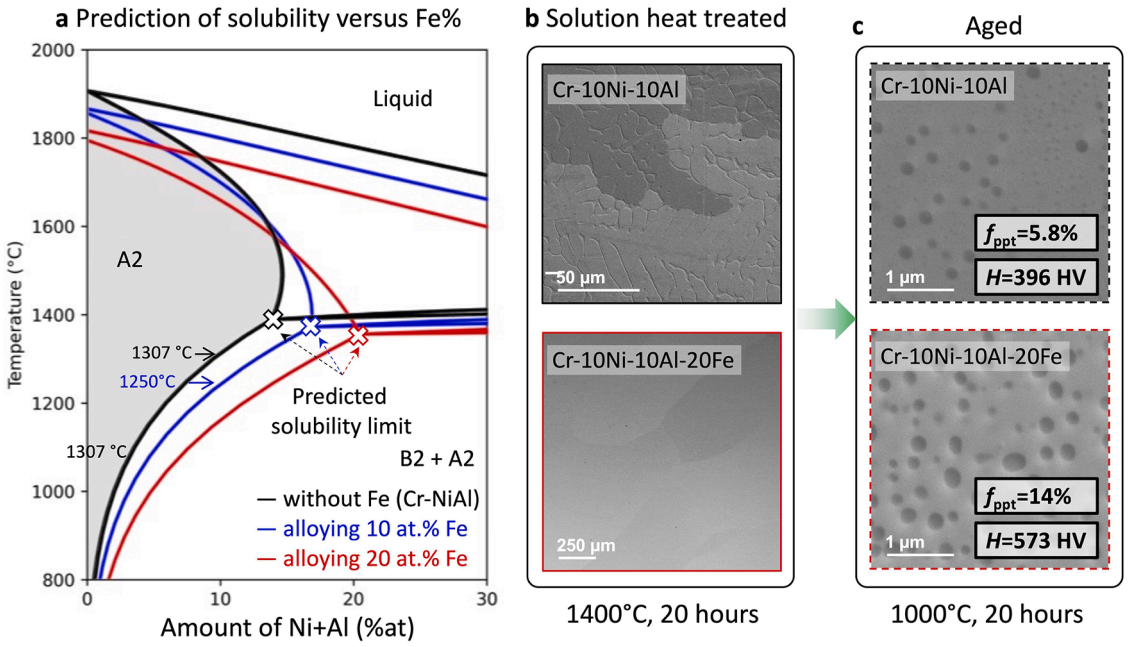

Fig. 3. (a) Predicted pseudo binary phase diagrams of Cr-NiAl and Cr(Fe)-NiAl using TCHEA-6 showing the effect of Fe addition on the solubility limit of Ni and Al as a function of Fe. The solubility limits shown by the cross are 14% at 1390 °C without Fe, 16.9% at 1374 °C with 10% Fe and 20.5% at 1357 °C with 20% Fe. Horizontal arrows pointing out solvus temperature for Cr-5Ni-5Al and Cr-5Ni-5Al-10Fe. (b) Microstructures of Cr-10Ni-10Al without Fe and with 20 at.%Fe after homogenisation at 1400 °C for 20 h. (c) Microstructure after ageing at 1000 °C for 20 h showing the area fraction of precipitates f_{ppt} and Vickers hardness, H, in Cr-10Ni-10Al and Cr-10Ni-10Al-20Fe.

measured using by APT, giving 98.7Cr-0.3Ni-0.9Al (A2) and 0.9Cr-52.7Ni-46.4Al (B2) (plotted in Fig. 2(b)). It is worth noting that the excess of Ni over Al in the B2 phase is consistent with tie lines in the ternary phase diagrams at 1200/1000 °C (Fig. S1). The A2-Cr solubility limit for Ni+Al limits the volume fraction of precipitates that can be produced. Increases in Ni and Al content beyond this limit promote grain

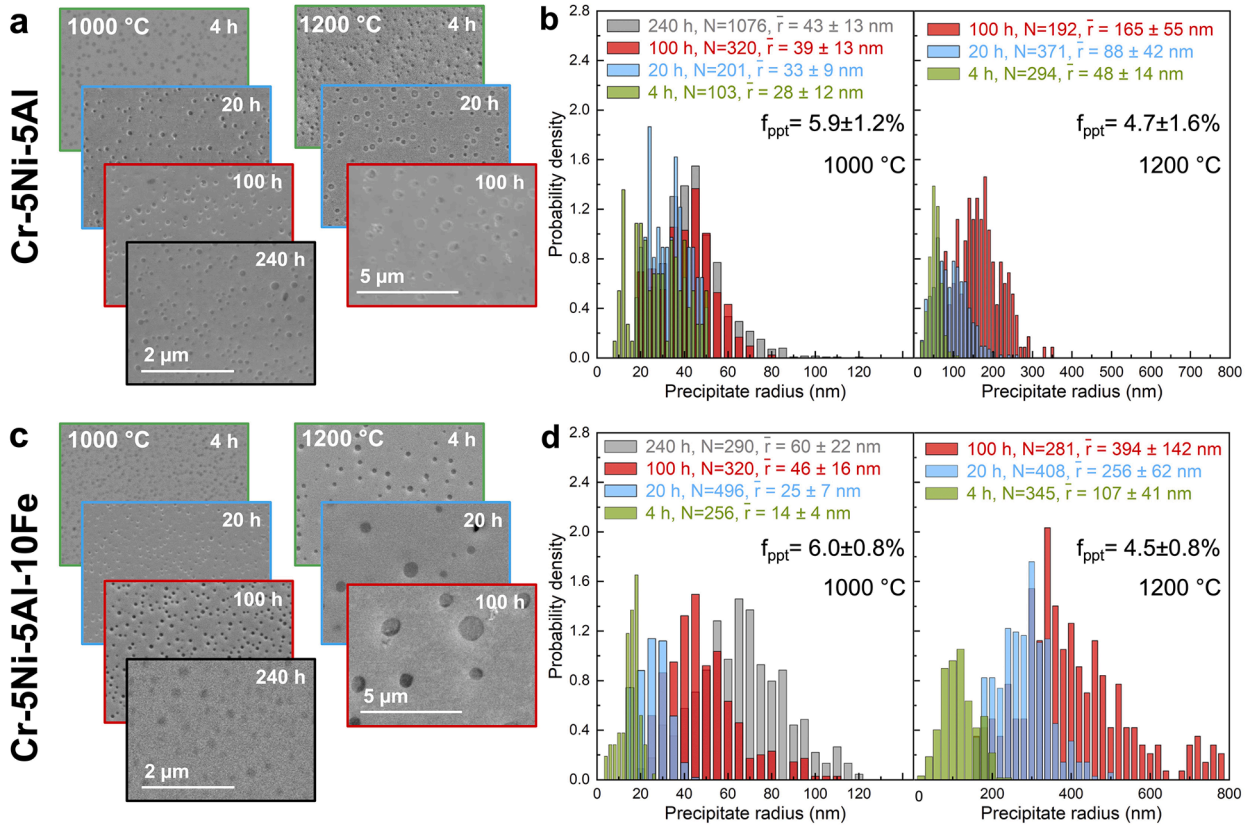

Fig. 4. Microstructure of (a) Cr-5Ni-5Al and (c) Cr-5Ni-5Al-10Fe aged at 1000 °C and 1200 °C for 4/20/100/240 h showing the coarsening of the precipitates with the corresponding precipitate size distribution in (b,d) respectively. f_{ppt} represents the area fraction of precipitate.

boundary precipitates and an interdendritic second phase, both of which are detrimental to ductility. Thus, increasing the A2 Ni+Al solubility for optimising the A2 solvus is a key alloy design point to enhance the precipitation volume fraction.

3.2. Effect of Fe on the phase diagram and microstructure

By alloying with Fe, the Cr matrix is modified to Cr(Fe) and the resulting solubility of Ni+Al is different. Fig. 3(a) presents the Cr-rich part of the pseudo-binary phase diagrams of Cr(Fe)-NiAl with different Fe contents. The solubility limit shifts from 14% at 1390 °C in the ternary to 16.9% at 1374 °C with 10% Fe addition, then to 20.5% at 1357 °C with 20% Fe addition. The solubility limit is predicted to increase with increasing Fe content. Experimentally, the microstructure of Cr-10Ni-10Al-20Fe can be completely homogenised without prior dendrites or grain boundary precipitates, in contrast to the dendritic microstructure in Cr-10Ni-10Al, Fig. 3(b). These experimental results are instructed by, and in agreement with, the CALPHAD calculation on the solubility of Ni+Al in the Cr(Fe) matrix. Furthermore, Fe additions increase the nano-scale precipitate volume fraction of 5.8% and hardness of 396 HV0.5 in Cr-10Ni-10Al to 14% and 573 HV0.5 in the Cr-10Ni-10Al-20Fe after ageing (Fig. 3c), enhancing the microstructural design of Cr-superalloys.

3.3. Precipitate coarsening during ageing

In the following part, the precipitate coarsening behaviour between the ternary Cr-5Ni-5Al and the quaternary Cr-5Ni-5Al-10Fe alloys is presented. These alloys were selected because they exhibit similar microstructures without dendrites and meet the superalloy design objective. In addition, the influence of Fe addition on the microstructure and properties of Cr-NiAl alloys could be evidenced by studying these two alloys. According to the pseudo-binary phase diagram in Fig. 2(b) and Fig. 3(a), the hardening precipitation treatment in the Cr-rich region can be carried out at temperatures lower than the solvus temperatures indicated in Fig. 3(a). The evolution of precipitates in Cr-5Ni-5Al and Cr-5Ni-5Al-10Fe alloys subjected to ageing at 1000 °C and 1200 °C is investigated. SEM images showing the microstructures are presented in Fig. 4(a,c). In both alloys and ageing temperatures, precipitates are embedded in the matrix and remain with a spherical morphology for all ageing times. The volume fraction is similar in all conditions, around 5.9 ± 1.2% (1000 °C) and 4.7 ± 1.8% (1200 °C) in Cr-5Ni-5Al and 6.0 ± 0.8% (1000 °C) and 4.5 ± 0.8% (1200 °C) in Cr-5Ni-5Al-10Fe. The corresponding precipitate size distribution with the number of precipitates and the mean radius is presented in Fig. 4(b,d).

Precipitates grow and coarsen during ageing as shown by the increase in the mean precipitate size as shown in Fig. 4. Here, it is reasonable to assume that coarsening is the predominant phenomenon under these heat treatments since the volume fraction for a given temperature in each alloy is small and similar for all ageing times. The coarsening kinetics of precipitates and the effects of alloying elements on the coarsening process of precipitates are important parameters to control the creep resistance of the alloys. Fig. 5(a) plots the increase of equivalent precipitate radius, $\bar{r}^3$, against the ageing time t. $\bar{r}$ is the mean radii of precipitates. Fig. 5(a) shows straight lines for the four cases with a positive intercept to the y-axis. The evolution of equivalent radius can thus be expressed as follows:

$$\bar{r}^3 - \bar{r}_0^3 = Kt \quad (3)$$

with K, the coarsening rate constant and $\bar{r}_0$ at the homogenised condition. This suggests that the precipitate coarsening in this study follows the diffusion-controlled coarsening rules by the Lifshitz-Slyozov-Wagner (LSW) theory, known as Ostwald ripening [50–52]. Comparing the Fe-free and Fe-containing alloys, as shown in Fig. 5(a), the addition of Fe increases the coarsening rate constant at both ageing temperatures.

Table 2
Lattice parameters of the A2 matrix and B2 precipitates measured by SXRD powder diffraction with the lattice misfit. The alloys are aged at 1000 °C for 20 h.

Alloys	a_{Cr} (pm)	a_{NiAl} (pm)	a_{A2} (pm)	a_{B2} (pm)	Misfit (%)
Cr-5Ni-5Al	288.5 [31]	288.7 [32]	288.54 (1)	288.95 (1)	0.142(6)
Cr-5Ni-5Al-10Fe	/	/	288.29 (1)	288.76 (1)	0.163(7)

Fig. 5(b) presents the coarsening rate constant of Cr(Fe)-NiAl alloys as a function of temperature. Surprisingly, it is noted that the coarsening rate constant of Cr(Fe)-NiAl alloys is by at least two orders of magnitude lower than the other common bcc-superalloys (ferritic alloys) [24,48,53–55] and fcc-superalloys (cobalt-based [56,57] and Ni-based [58–62]) to date (Fig. 5(b)), even though the Fe addition increases the coarsening rate slightly. The remarkably low coarsening rates demonstrate unprecedented microstructural stability at high temperatures, which is optimal for creep resistance and ensures a longer service life of the alloy.

3.4. Ageing-hardness relation and stress-strain response

Fig. 6 shows the Vickers hardness of Cr-5Ni-5Al and Cr-5Ni-5Al-10Fe aged at 1000 °C as a function of the ageing time. Both ternary and quaternary alloys show highly improved hardness compared to pure Cr of which the hardness is measured to be ~150 HV. The hardness of the quaternary alloy (> 500 HV) is higher than IN718 (300–400 HV), pure W (400–450 HV) and comparable to some new W-based alloys [29]. The quaternary alloy is harder than the ternary, which is attributed to the recombination of both precipitate strengthening and solid solution strengthening by Fe in the matrix. Both alloys show age-softening (hardness decrease with the ageing time), suggesting a softening lead by the coarsening process. Interestingly, the quaternary alloy exhibits reduced age softening compared to the ternary alloy.

Compression tests at various temperatures were performed to investigate the stress-strain response of Cr-5Ni-5Al and Cr-5Ni-5Al-10Fe (aged at 1000 °C for 20 h). Samples were compressed to failure or up to 60% of their original length. Fig. 7 presents the results of up to 20% deformation at 24/300/450/800/900/1000 °C. The compression of the ternary alloy at room temperature and 1000 °C was repeated and showed good reproducibility so here only a single curve is plotted. The compression of Cr-superalloys alloyed with Fe exhibit higher strength than the ternary alloys, with yield stress ~1.3 GPa at room temperature, and can retain its high strength (~320 MPa) at 1000 °C. Both alloys show compressive ductility to some extent at RT and 300 °C but cracking occurred during the deformation. It is worth noting that cracking occurs for temperatures < 450 °C with jags observed in the stress-strain curves. The cracking leads to a drop of stress which causes a lower stress at 300 °C than at 450 °C for Cr-5Ni-5Al-10Fe. At temperatures > 800 °C, the alloys exhibit smooth deformation.

3.5. Microstructure characterisation of Cr(Fe)-NiAl (1000 °C, 20 h)

A ternary and a quaternary alloy under one ageing condition were selected for further microstructural characterisation. In both aged alloys, A2 and B2 structures are identified using SXRD (Fig. 8). The two phases correspond to the A2 Cr-rich matrix and the nano-scale spherical B2-NiAl precipitates (homogeneously distributed through the matrix according to SEM observations). Some extra peaks are not considered in the analysis as they appeared after the powder annealing treatment (stress relief treatment), suggesting that they are from oxides formed during the annealing. The lattice parameters are measured based on the Rietveld refinement and listed in Table 2 with a lattice misfit of 0.142

Table 3
Composition (at.%) of Cr-5Ni-5Al-10Fe and Cr-5Ni-5Al alloys (measured by SEM-EDS) and of constitutive phases (matrix and B2 precipitates) after ageing at 1000 °C for 20 h (as determined by APT, all in at.%). Volume fraction deduced by the Lever rule is also given. Uncertainties are represented by the standard deviation(s) from the mean values of multiple APT tips.

Alloys	Phase	Cr	Ni	Al	Fe	$\overline{\phi}_{\beta'}$ by APT	$\overline{\phi}_{\beta'}$ by SEM
Quaternary	nominal	80.8 ± 0.1	4.6 ± 0.1	5.1 ± 0.1	9.5 ± 0.1		
	matrix	86.1 ± 0.3	1.2 ± 0.1	1.4 ± 0.1	11.2 ± 0.3		
	precipitate	0.9 ± 0.2	51.2 ± 0.3	44.1 ± 0.2	3.7 ± 0.1	7.5 ± 0.3	6.0 ± 0.8
Ternary	nominal	89.7 ± 0.5	5.5 ± 0.3	4.8 ± 0.3	/		
	matrix	98.7 ± 0.1	0.3 ± 0.1	0.9 ± 0.1	/		
	precipitate	0.9 ± 0.3	52.7 ± 0.5	46.4 ± 0.5	/	8.9 ± 0.2	5.9 ± 0.3

±0.006% and 0.163±0.007% in the ternary and quaternary alloys respectively. The XRD results show a low effect of Fe addition on the A2 and B2 lattice parameters and in consequence a small influence on the lattice misfit.

Diffraction patterns using TEM in Fig. 9(b) show that the precipitates have a cube-cube orientation relationship ($<001>_{A2}//<001>_{B2}$, $\{100\}_{A2}//\{100\}_{B2}$) with the matrix, same as the observation in a Fe-free Cr-NiAl alloy [27]. The precipitates and matrix are highly coherent with the diffraction spots of the A2 and B2 phases completely superimposed except the B2 superlattice reflections. HR-STEM observations (Fig. 9(d)) also reveal that their interface is coherent. No dislocations could be found in Fourier-masked micrographs using {200} and {110} orientation. Across the interface of the precipitate (diameter about 60 nm) shown in Fig. 9(c), only two interfacial dislocations are detected in a {112} orientation as shown in Fig. 9(g). It is worth to mention that there are two types of artefact objects observed by TEM as shown in Fig. 9c. The first type is some barely visible dark spots of < 1 nm in the NiAl precipitate, likely FIB-induced damage. The second type is some white spots of < 10 nm across the image and sample, assumed to be the oxidation of the sample. The white spots with size of about 10 nm in Fig. 9(c) are related to the oxidation of the sample.

Fig. 10(a,b) shows the element distribution in an exemplar APT sample of the quaternary and ternary alloy. The composition of the matrix and the precipitates of Cr-5Ni-5Al-10Fe and Cr-5Ni-5Al aged at 1000 °C for 20 h was determined across numerous samples, comprising more than 150 million ions per condition. As expected, Ni and Al are enriched in the β' precipitates demarcated by 25% Ni isoconcentration surfaces. Fe mainly partitions to the matrix and is only slightly incorporated into the intermetallic precipitates. The concentration profiles of the major elements across the interfaces are shown in Fig. 10(c) by means of proximity histogram analyses. Proximity histograms show the chemistry as a function of distance from an interface as defined by an isoconcentration surface. Cr, Ni and Al show similar behaviour across the interface in both alloys with a transition width of less than 2 nm. In the quaternary alloy, a slight enrichment of Fe at the interface can be observed. Further, alloying with Fe slightly increases the Ni and Al content measured in the matrix compared to the ternary alloy. The results of the phase compositions are summarised in Table 3.

The phase composition also allows the determination of the β' volume fraction $\phi_{\beta'}$ using the Lever rule:

$$\boldsymbol{C}_{n,i} = \phi_{\beta'}\boldsymbol{C}_{\beta',i} + (1-\phi_{\beta'})\boldsymbol{C}_{\beta,i} \tag{4}$$

where $\boldsymbol{C}_{n,i}$ is the nominal concentration of the species i, $\boldsymbol{C}_{\beta',i}$ and $\boldsymbol{C}_{\beta,i}$ are the concentrations of the species i in the precipitate and the matrix respectively. The plot of $\boldsymbol{C}_n - \boldsymbol{C}_\beta$ *versus* $\boldsymbol{C}_{\beta'} - \boldsymbol{C}_{\beta,i}$ should yield a straight line with the gradient equal to the volume fraction $\phi_{\beta'}$. The average $\overline{\phi}_{\beta'}$ is calculated to be 7.5% as given in Table 3. The volume fraction by APT is consistent with the SEM observation; the SEM observations suggest 6% precipitate volume fraction which is slightly lower than the value by APT but in reasonable agreement with the uncertainty.

In the Cr-5Ni-5Al alloy, both large and small precipitates are observed with comparable composition. The small precipitates are assumed to form during cooling, which suggests again that the addition of iron increases the solubility of Ni and Al and suppresses the formation of secondary precipitates during the quenching. The volume fraction calculated using the Lever rule is 8.9% in the ternary alloy. This agrees well with the results obtained by SEM, as $\phi_{\beta'}$ determined by APT represents the sum of all β' phases including the ageing-induced precipitates (measured as 5.9% in Fig. 4(b)) and secondary B2 phase at grain boundaries (measured as 4% in Fig. 1).

4. Discussions

4.1. Assessment of the Cr-rich region in the Cr-Ni-Al system

The Cr-Ni-Al ternary system is of interest for both Ni-based and Al-based alloys, especially for high-temperature applications such as turbine blades or nuclear reactors. Therefore, previous thermodynamic assessments of the ternary system have focused on the Ni-rich region, resulting in a well-established phase diagram in the Ni-rich corner [63,64]. Recently, detailed experimental investigations of the Al-rich part of the system have been reassessed which leads to a new description of the Al-Cr system and Al-Cr-Ni system [40]. Furthermore, new thermodynamic assessments have been conducted on NiAl-Cr eutectic alloys which were approaching the Cr-rich corner [65,66]. These works to date have narrowed the Cr-rich A2 region but detailed experimental descriptions are still limited to [41,42]. The compositions of A2 and B2 phases at 1200/1000 °C with new tie lines have also been plotted in the ternary phase diagrams (Fig. S1), showing that the A2 single-phase area is overestimated by the current thermodynamic database. In this work, new experimental data in the Cr-rich corner in the Cr-Ni-Al system is presented for further completeness and understanding of the phase diagram.

Along with the addition of Fe, their influence on the solubility of Ni+Al is demonstrated while the thermodynamic foundation of this effect requires further modelling investigations. The Cr-NiAl alloys tailored by Fe supplements provide a new design foundation for Cr-superalloys. As shown in Fig. 3(b,c), the aged Cr-10Ni-10Al-20Fe alloy also meets the "superalloy design objective", and it will have a higher precipitate volume fraction than Cr-5Ni-5Al-10Fe, which may lead to a different creep behaviour and will be of interest for high-temperature mechanical tests. The comparative study on Cr-5Ni-5Al-10Fe in relation to Cr-5Ni-5Al aims to investigate the effect of Fe additions on the precipitate coarsening and microstructure. Furthermore, a comprise amongst precipitate volume fraction, coarsening rate and strengthening should be considered when selecting the alloy composition in the future.

4.2. Interface energy and coarsening kinetics

A coherent interface is expected to provide a better creep resistance [25]. The properties of coherent/semi-coherent precipitates, *e.g.* their coarsening and morphology, are controlled by two key parameters: misfit strain and interfacial energy, $\boldsymbol{\gamma}$. In Cr(Fe)-NiAl alloys, the low lattice misfits shown in Table 2 indicate a low misfit strain, consistent with the morphology, which remains spherical even at diameters closer

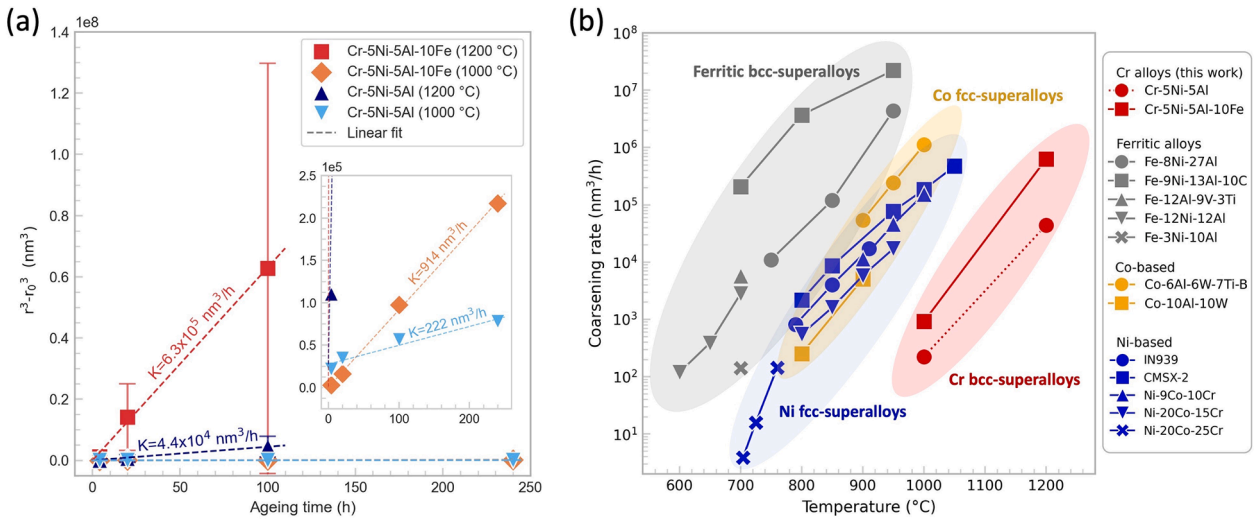

Fig. 5. (a) Plot of r^3-r_0^3 *versus* ageing time for coarsening rate determination. (b) Coarsening rate as a function of the ageing temperature of Cr-superalloys, some ferritic superalloys [24,48,53–55], Co-based superalloys [56,57] and Ni-based superalloys [58–62]. The error bar shows the standard deviation of measured data.

Table 4
Coarsening rate constants (from Fig. 6a) and interfacial energies in Cr-5Ni-5Al (ternary) and Cr-5Ni-5Al-10Fe (quaternary) alloys aged at 1000 °C and 1200 °C.

Alloy systems	Ternary		Quaternary	
Ageing temperature T, (°C)	1000	1200	1000	1200
K (nm^3/h)	222 ±38	4.4 ± 0.2 x10^4	914 ±26	6.3 ± 0.3 x10^5
γ (mJ/m^2)	37±6.5	21±0.8	39±1.7	18±0.5

to micrometres. These observations suggest that the interfacial energy dominates the precipitate morphology compared with the misfit strain and that the interface energy should be isotropic at 1000 °C and 1200 °C. Precipitates with high misfit strain tend to have a cuboidal shape as they align their interface with some specific lattice planes to minimize the elastic strain induced by the misfit [55,67]. Consequently, $\boldsymbol{\gamma}$ should be dominating over misfit strain on the precipitate coarsening and morphology. However, data on the interface energy in the Cr-NiAl system is rare. Wu *et al.* reported an interface energy $\boldsymbol{\gamma}_{(110)}$ of 580 mJ/m^2 in the Cr-NiAl system by means of the density functional theory [68]. Here, the interface energy is determined experimentally by means of the coarsening kinetics. The coarsening rate in multi-component systems can be approximated as: [69]

$$\boldsymbol{K} = \frac{8\boldsymbol{\gamma}\boldsymbol{V}_m^{B2}}{9\boldsymbol{RT}\sum_i^N (\boldsymbol{c}_i^{B2} - \boldsymbol{c}_i^{A2})^2 \Big/ \boldsymbol{D}_i^{A2}\boldsymbol{c}_i^{A2}} \tag{5}$$

where $\boldsymbol{\gamma}$ is the interfacial energy; $\boldsymbol{V}_m^{B2}$, the molar volume of NiAl; $\boldsymbol{R}$, the gas constant; $\boldsymbol{T}$, the temperature; and $\boldsymbol{c}_i^j$ and $\boldsymbol{D}_i^j$, the atomic fraction and diffusion coefficient of solute, *i*, (Ni, Al or Fe) in the phase j (A2 or B2), respectively. Diffusion coefficients are calculated using the TCMOB2 database in Thermocalc. Phase compositions are measured by STEM-EDS and APT.

The interface energy is thus proportional to the coarsening rate. Here, the coarsening rates and their uncertainty are determined experimentally using the linear regression function of the Origin software as shown in Fig. 5 and Table 4. Interface energy is then deduced using the parameters in Fig. 11 and presented in Table 4. The values of $\boldsymbol{\gamma}$ in the quaternary and ternary alloys are similar and are temperature dependent of about 20 mJ/m^2 at 1200 °C and 40 mJ/m^2 at 1000 °C, respectively. These results do not reflect a change of $\boldsymbol{\gamma}$ due to Fe addition. It should be noted that the phase concentration and diffusion coefficients affect the value of $\boldsymbol{\gamma}$. Here, the determination of phase composition by APT depends on the decomposition method, which causes a slight variation of Al and Fe content in the matrix. Nevertheless, the driving force controlling the interface value is the term of Ni $(\boldsymbol{c}_{Ni}^{B2} - \boldsymbol{c}_{Ni}^{A2})^2/\boldsymbol{D}_{Ni}^{A2}\boldsymbol{c}_{Ni}^{A2}$ with two orders of magnitude higher than the Al and Fe. Thus, the choice of the decomposition method does not affect the interface energy value. However, the value of Ni diffusion coefficient $\boldsymbol{D}_{Ni}^{A2}$, will significantly affect the results as it is proportional to $\boldsymbol{\gamma}$. The accuracy of the diffusion coefficients is beyond the scope of this study.

The $\boldsymbol{\gamma}$ measured in Cr(Fe)-NiAl alloys are similar to experimentally reported values of 10–48 mJ/m^2, in Fe-based [48,54], Ni-based [70,71] and Co-based [72] superalloys for temperatures between 700 and 900 °C. But the measured values in Cr-NiAl systems are one order of magnitude lower than the modelling result from Wu et al. [68]. On the one hand, the discrepancy could be due to the uncertainty of diffusion coefficients. On the other hand, the $\boldsymbol{\gamma}$ calculated by DFT did not consider the temperature effects and the composition transition at the interface. The inconsistency on $\boldsymbol{\gamma}$ between modelling and experiments is also observed in other alloy systems such as Fe-NiAl [48].

Given that $\boldsymbol{\gamma}$ across the different systems are similar, what is the origin of the exceptionally low coarsening rate in Cr(Fe)-NiAl alloys compared to other superalloy systems? Based on Eq. (5), the dominating terms controlling the coarsening rate comprise the difference in solute concentration between matrix and precipitates $\Delta\boldsymbol{C}_i = (\boldsymbol{c}_i^{B2} - \boldsymbol{c}_i^{A2})^2/\boldsymbol{c}_i^{A2}$ as well as the diffusivities of solute atoms $\boldsymbol{D}_i^{A2}$. The coarsening rate decreases with the increase in $\Delta\boldsymbol{C}_i$ and decrease in $\boldsymbol{D}_i^{A2}$. The Cr-superalloy with Fe additions (Cr-5Ni-5Al-10Fe aged at 1000 °C) is compared to a ferritic superalloy FBB8 at 950 °C [48], a Ni-superalloy IN939 at 816 °C [73] and a Co-superalloy at 950 °C [57,72]. Phase compositions in the latter three alloys are presented in [48,57,73] and the diffusion coefficients are given or deduced from [48,74,75]. Fig. 11(a,b) plot the difference in concentration of the major elements between the matrix and precipitate and their diffusion coefficients respectively in each alloy. For most solutes in all the alloy systems, the difference in concentration is within one order of magnitude from 0.1 to 1. However, $\Delta\boldsymbol{C}_i$ of Ni and Al in the Cr-superalloy are higher than 10, suggesting a strong partitioning of Ni and Al in the precipitates. The low solute concentrations in the matrix should suppress the precipitate coarsening. The solute diffusivities $\boldsymbol{D}_i^{A2}$ in the Cr-superalloy are much lower than the ones in the ferritic and cobalt superalloy except Al but are higher than the ones in Ni-superalloy. Note that the diffusion coefficients in the Ni-superalloy is low as the temperature is about 150–200 °C lower than the others.

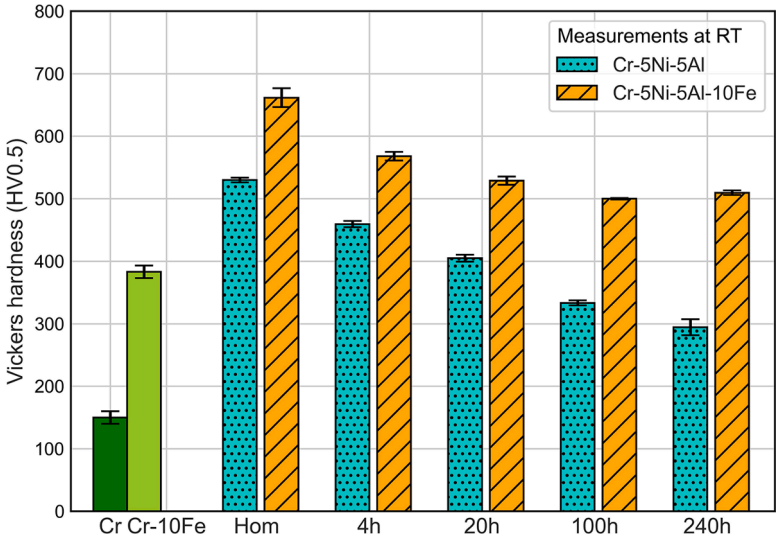

Fig. 6. Vickers Hardness (HV) of Cr-10Fe (matrix), Cr-5Ni-5Al and Cr-5Ni-5Al-10Fe under different heat treatment conditions and ageing at 1000 °C. Hardness was measured at room tempreature (RT).

Fig. 11(c) presents the sum of $\Delta C_i/D_i^{A2}$ which drives the precipitate coarsening. The value in the Cr-superalloy is much higher than that of the Fe and Co systems for a comparable temperature. It is interesting to note that the value in Fig. 11(c) in Cr-superalloy at 1000 °C is similar to that in Ni-superalloys at 816 °C. It suggests that the interface energy in Cr-superalloys should be similar to the value in Ni-superalloys since Cr-superalloys at 1000 °C show comparable coarsening behaviour to Ni-superalloys at 800 °C as shown in Fig. 5(b). It is also worth mentioning that adding Fe increases the Ni and Al solubility which thus reduces ΔC_i. As the Fe addition has a minor effect on the interface energy, the reduction of ΔC_i increases the coarsening rate as observed experimentally. By adding Fe as supplement, a compromise between the solubility and microstructure thermal stability needs to be considered.

4.3. Mechanical properties of Cr-superalloys

It is worth reminding that the "bcc-superalloy" design is intriguing for creating alloys with high strength at room and high temperatures. Here the compressive strength of Cr-superalloys is compared with the tensile strength of some novel alloys and some commercial superalloys. The compression test provides a useful first investigation of the strength of novel alloys and, thus, is a common way to determine the yield strength of bcc alloys with coherent precipitation in the early stages of development *e.g.* [76–79]. However, it is worth mentioning that the compressive strength could differ from the tensile strength of brittle materials. The compression stresses of Cr-superalloys offer a fair comparison with tensile stresses of commercial alloys in temperatures above their DBTT (*e.g.* at > 800 °C). The Cr-superalloy design offers a significant improvement of strength at T > 800 °C compared to pure Cr, a Ni-superalloy (Inconel 718) [80], and a Co-superalloy [81] as shown in Fig. 12. Although the CMSX-4 Ni-superalloy show higher yield strength than Cr-superalloys (Fig. 13) at T > 800 °C, a large amount of refractory elements including rhenium (~3%), tantalum (> 5%) and tungsten (> 5%) are alloyed into CMSX alloys to achieve their exceptional high-temperature strength. In addition, Cr-superalloys also exhibit high strength compared to some novel alloys such as Fe-superalloys (ferritic superalloy FBB8) [82] and refractory alloys (vanadium-based [83], tantalum-based alloys [84]) and comparable to some refractory high-entropy alloys (RHEA) such as $Hf_{15}Nb_{40}Ta_{25}Ti_{15}Zr_5$ [36].

In addition to their strength, the ductility of alloys should also be addressed. The compression tests in the present work demonstrate that the Cr(Fe)-NiAl alloys preserve, to some extent, ductility at temperatures > 800 °C, which validates the alloy design, while other novel intermetallic-strengthened Cr alloys such as Cr(Mo)-Cr_3Si alloys were

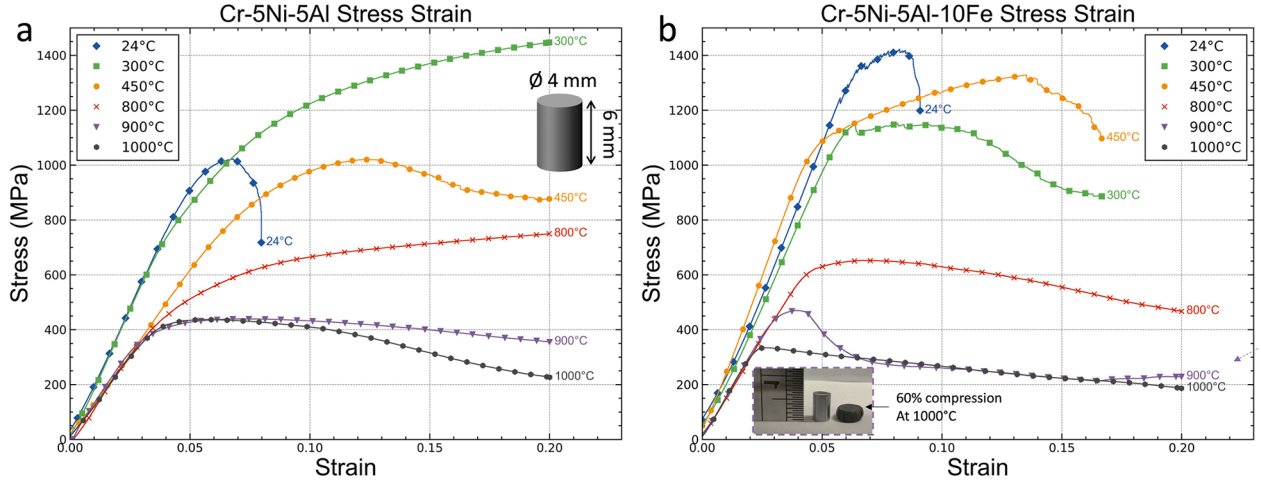

Fig. 7. Strain-stress response of Cr-5Ni-5Al and Cr-5Ni-5Al-10Fe aged at 1000 °C for 20 h under compression from room temperature to 1000 °C with a strain rate $3.3\times10^{-4}\ s^{-1}$.

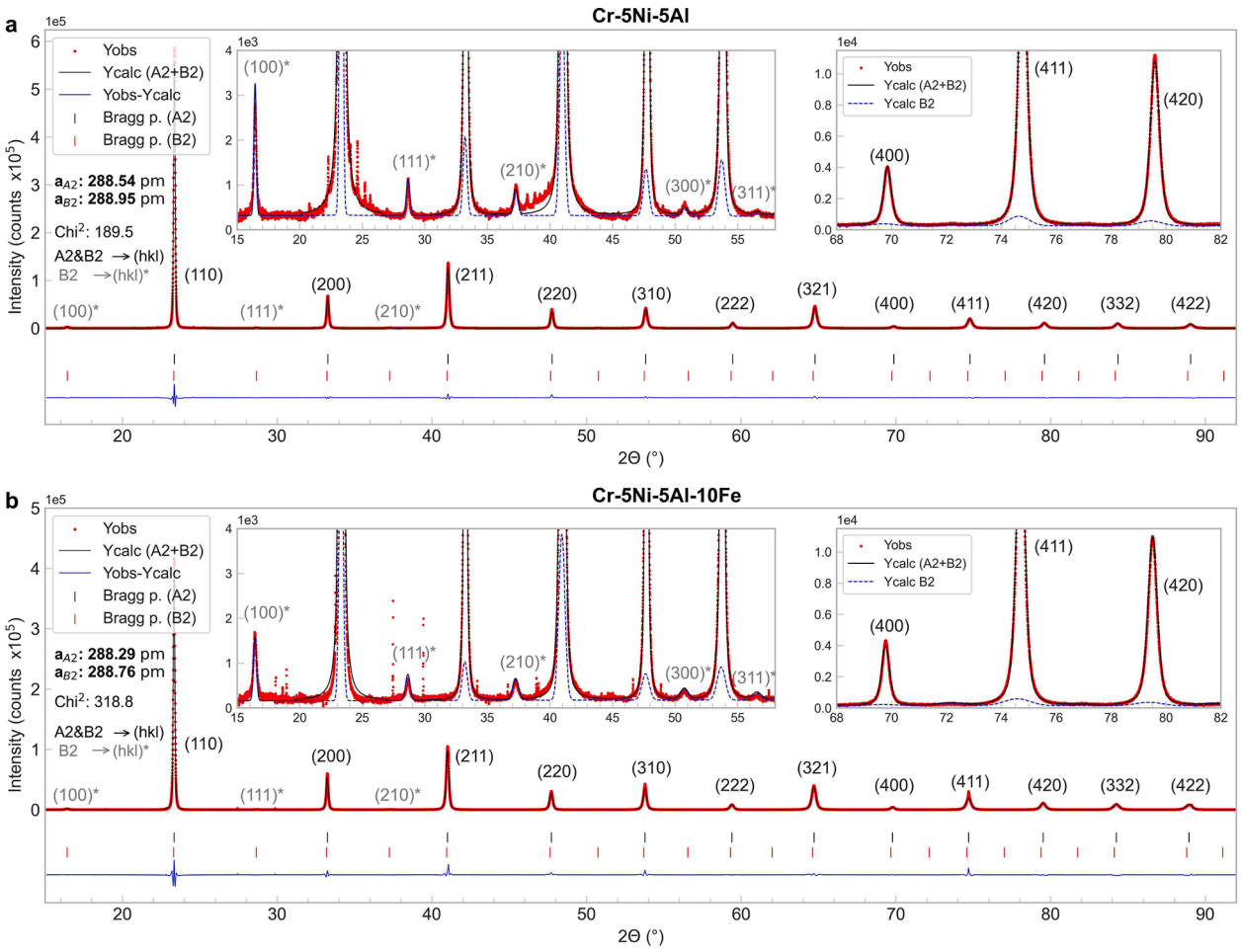

Fig. 8. Synchrotron powder X-ray diffraction (SXRD) patterns of (a) Cr-5Ni-5Al and (b) Cr-5Ni-5Al-10Fe aged at 1000 °C for 20 h (λ = 82.6596 pm). The extra superlattice reflections from B2 ordering are indicated with an asterisk with at least 5 peaks observed as shown in the left inset graphs. Extra oxide peaks due to powder heat treatment are shown in left inset graphs. Overlap of A2 and B2 peaks with B2 contribution is shown at high angle peaks in right inset graphs.

shown to be brittle below 1227 °C [85]. The quaternary alloy shows similar ductility as the ternary, although the addition of Fe is expected to improve the ductility. However, in both quaternary and ternary alloys compressed at > 800 °C at which the alloys are ductile, surface cracking is observed, suggesting that these alloys are surface-notch sensitive [16]. Tensile tests would be more appropriate than compression to evaluate the ductility of alloys. However, our focus is on the high-temperature yield strength to which the microstructure tends to lead. Without prior thermo-mechanical processing, the studied alloys tend to have a high DBTT like most early-stage bcc alloys with a coherent precipitation [86–89]. Meanwhile the microstructure resulting from the casting (pores) and homogenisation (millimetric grain sizes) can also result in a high DBTT [90]. Further ductilisation of the Cr-superalloys could be addressed via solute additions *e.g.* increasing the Fe content, adding vanadium/cobalt/silver into the matrix [91,92] and substituting Ni or Al with Cr/vanadium/manganese to reduce the antiphase boundary energy to encourage slip within the NiAl intermetallic [93].

4.4. Strengthening mechanisms

The hardness (Fig. 6) of the aged Cr-5Ni-5Al-10Fe samples reflected a softening up to 100 h and a constant value for longer times (240 h). The understanding and further microstructural optimisation require an analysis on the operating strengthening mechanism. The strengthening in the quaternary alloy is attributed to the solid solution strengthening and precipitate strengthening. The grain boundary strengthening is neglected due to the large grain size (*ca.* 1 mm) also indentations were performed far from grain boundaries. The increase in shear stress, $\Delta\boldsymbol{\tau}_{exp}$, due to particle strengthening in Cr-5Ni-5Al-10Fe is approximated as:

$$\Delta\boldsymbol{\tau}_{exp} = \frac{\left(\boldsymbol{\sigma}_{ys}^{H} - \boldsymbol{\sigma}_{ys}^{H,mat}\right)}{3\boldsymbol{M}} = \frac{(\boldsymbol{H} - \boldsymbol{H}_{mat})}{11.4\boldsymbol{M}} \tag{6}$$

where $\boldsymbol{\sigma}_{ys}^{H}$ and $\boldsymbol{\sigma}_{ys}^{H,mat}$ are the yield stress of the alloy and A2 matrix, respectively, estimated from Vickers micro-hardness using Tabor's empirical equation [95], $\boldsymbol{\sigma}_{ys}^{H} = \boldsymbol{H}/\boldsymbol{n}$, with $\boldsymbol{H}$ being the hardness of the alloy in GPa and $\boldsymbol{n} = 3.8$ a constant deduced from the experimental hardness (5.2 GPa) and compression yield stress (1.3 GPa) at room temperature; $\boldsymbol{M} = 2.9$ is the Taylor factor for bcc materials [96]. The hardness of the matrix of the quaternary alloy $\boldsymbol{H}_{mat}$ is measured as the hardness of the Cr-10Fe binary alloy, about 310 HV in agreement with other experiments [20]. The experimental results of $\Delta\boldsymbol{\tau}_{exp}$ deduced from the hardness are plotted in scattered points in Fig. 13 as a function of the mean precipitate radius in the alloy aged at 1000 °C for 4/20/100/240 h.

There are several mechanisms of coherent precipitate strengthening, within which, depending on their nature, they can operate simultaneously or compete for dominance [97–99]. Since their operation is associated with the precipitate size, it is useful to plot their different dominance ranges as a function of the precipitate radius. In this work, only the strengthening mechanisms identified as relevant for the quaternary alloy are presented. These are grouped according to the following operation radius ranges: (i) $\Delta\boldsymbol{\tau}_{pcd}$ cutting by strong

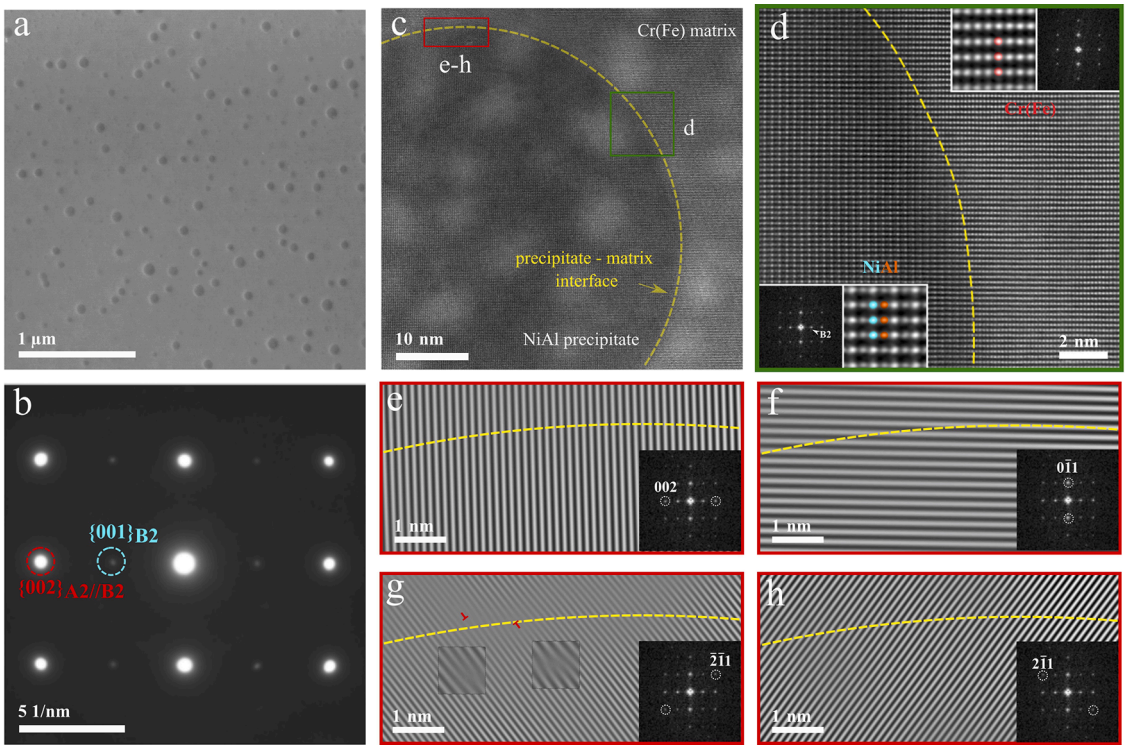

Fig. 9. Microstructural characterisation of Cr-5Ni-5Al-10Fe aged at 1000 °C for 20 h. (a) SEM secondary electron micrograph showing the general matrix-precipitate microstructure. (b) TEM diffraction patterns along <011> zone axis showing the cube-to-cube orientation between the matrix and precipitates. (c) High angle annular dark field (HAADF) STEM image along <110> zone axis with yellow dashed line highlighting the precipitate boundary. (d) Atomic scale HAADF-STEM images with inset images showing the corresponding details of each crystal lattice and reduced Fast Fourier Transforms (rFFTs), with fields-of-view of 1.29 nm and 27.7 nm^{-1}, respectively. (e-h) Fourier-masked micrographs acquired from the red rectangle area in (c) showing the highly coherent interface structure with interfacial dislocations detected only using a <211> reflection.

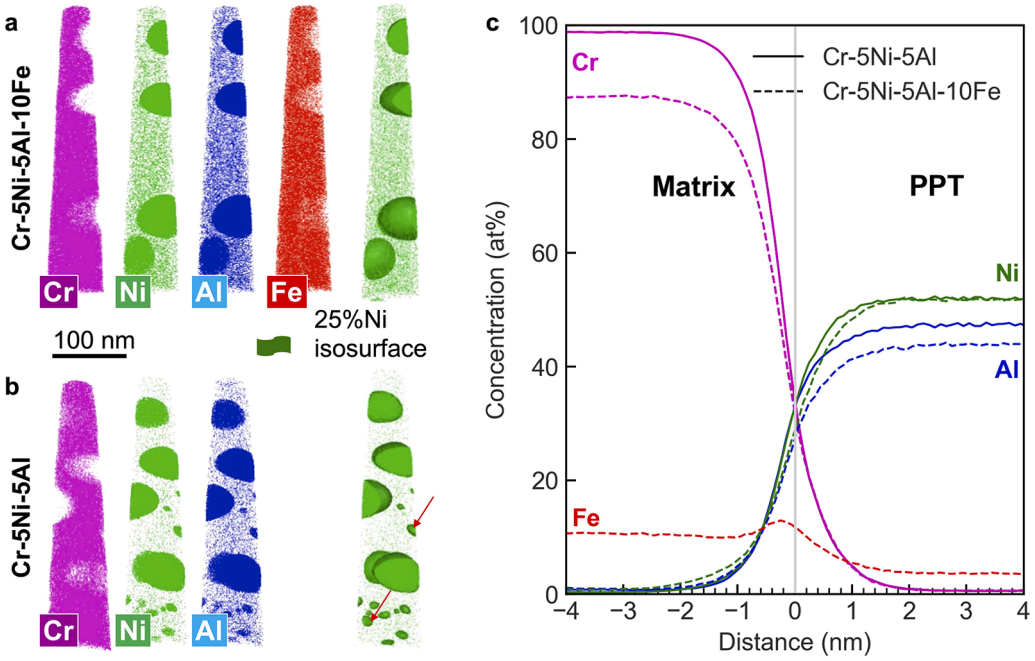

Fig. 10. Atom maps showing the distribution of the major elements with precipitate/matrix demarcated using 25% Ni isosurfaces along in (a) Cr-5Ni-5Al-10Fe and (b) Cr-5Ni-5Al aged at 1000 °C for 20 h with (c) the partitioning of elements across the precipitate/matrix interface using proximity histograms.

pair-coupled dislocation (PCD) interacting with anti-phase boundaries [100–102] also known as order strengthening, (ii) $\Delta\tau_{m+c}$ strengthening by modulus and coherency hardening [102–104], and (iii) $\Delta\tau_{Or}$ Orowan bypassing [105,106]. The experimental data obtained in this work, including the precipitate size and lattice misfit, combined with data in the literature, allow the calculation of the value by each mechanism. It is

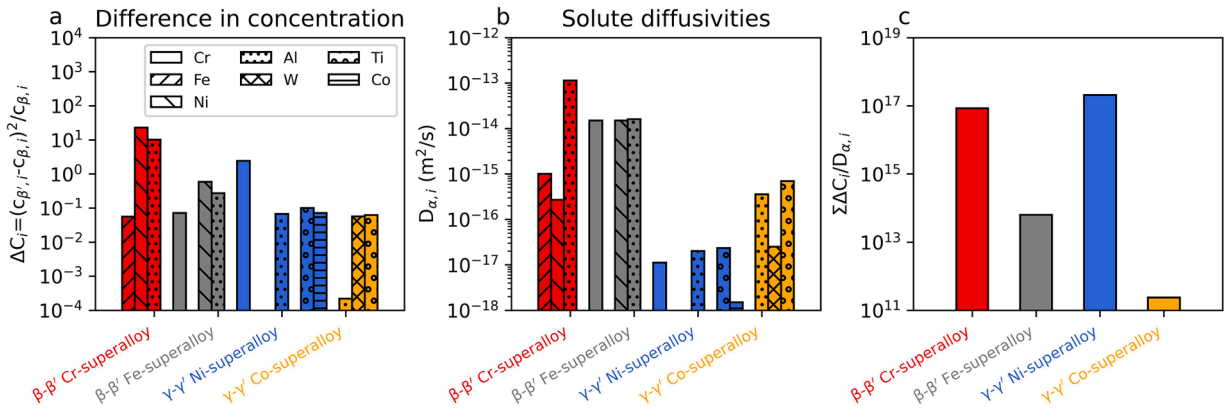

Fig. 11. Contribution of (a) solute concentration difference between the matrix and precipitates and (b) diffusivities of solutes on the precipitate coarsening rate in the $\beta-\beta'$ Cr-superalloy (Cr-5Ni-5Al-10Fe), a $\beta-\beta'$ Fe superalloy FBB8 (Fe-12.7Al-9Ni-10Cr-1.9Mo [48]), a $\gamma-\gamma'$ Ni-superalloy (IN939, Ni-25Cr-18Co-4Al-4.4Ti [73]) and a $\gamma-\gamma'$ Co-superalloy (Co-5.6Al-5.8W-6.6Ti [57]). The base element and solutes <2 at.% are not considered. (c) is the recombination of (a) and (b) driving the coarsening of precipitates as the denominator in Eq. (5).

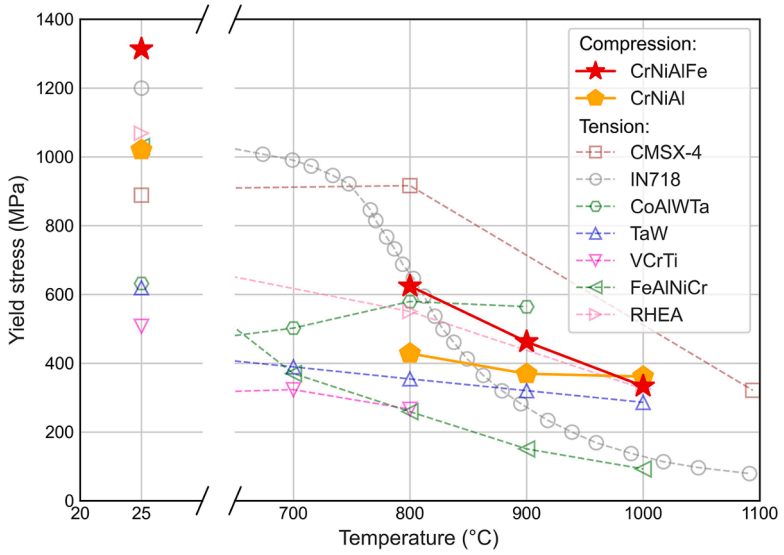

Fig. 12. Room to high-temperature compression 0.2% yield stress of Cr-superalloys compared to the tensile yield stress of other alloys for high-temperature uses, including typical fcc Ni-superalloys (IN718 [80] and single-crystal CMSX-4 [94]), fcc Co-superalloy (Co-Co_3(Al, W)-Ta alloy [81]), bcc ferritic superalloy (Fe-NiAl-Cr [25]), refractory alloys (tantalum-based alloys [84], vanadium-based alloys [83], and novel refractory high-entropy alloys (RHEA) $Hf_{15}Nb_{40}Ta_{25}Ti_{15}Zr_5$ [36]).

worth noting that most models are suitable for "simple" microstructure with dispersive spherical (semi-)coherent precipitates where the quaternary alloy fulfils the assumptions. But the analysis in the ternary alloys involves the secondary B2 phase at grain boundaries (Fig. 1) and a bimodal distribution of precipitate sizes (Fig. 4(b)) so it is not analysed here.

For the first mechanism, order strengthening can occur when a dislocation in the matrix shears an ordered-phase precipitate. When the dislocation slips across the precipitate, it will create an Anti-Phase Boundary (APB), representing the force per unit length against the dislocation. A second dislocation moving on the same plane as the first one can partially remove the APB which reduces the energy of the system. Here we consider dislocations with a Burgers vector $b = a/2<111>$ slipping on a close-packed plane [109,110]. The increase in shear strength by ordering strengthening can be deduced as [100–102]:

$$\Delta\tau_{pcd} = \left[\frac{0.83}{2}\frac{wT\phi^{0.5}}{br}\left(\frac{\pi^2}{4}\frac{\gamma_{APB}r}{wT}-1\right)^{0.5}\right]\times[0.94(1+C_{SL}\eta_{SL})] \quad (7)$$

where w is the fitting parameter accounting for the elastic repulsion between the paired dislocations outside the particles and is determined by fitting the experimental data (0.22) [107]; T is the dislocation line tension ($Gb^2/2$=3.27 GPa is the dislocation line tension with G=105 GPa is the shear modulus of the A2 matrix (~10%Fe) [108]); ϕ is the precipitate volume fraction; b is the Burgers vector ($|\frac{a}{2}\langle 111\rangle|$=0.2496 nm, with a = 0.28829 nm the lattice parameter of Cr); r is the precipitate radius (nm); γ_{APB} is the anti-phase boundary energy (800 mJ/m^2 [2]); C_{SL}=3 a constant for spherical precipitates; $\eta_{SL} = \phi^{0.5}/2$ for the effective mean planar particle-spacing estimations based on [100,101]; and A=0.72 for spherical precipitates. The weak PCD model is not considered here since it dominates for a precipitate radius below 5 nm.

For the second operation mechanism, the modulus and lattice mismatch contribute to the increase in shear strength as a precipitate shearing mechanism. Note that the strengthening by order strengthen achieves the maxima when the dislocation arrives at the centre of the intersection of the glide plane, while the strengthening by modulus and lattice mismatch reaches the peak when the dislocation touches the precipitate. The yield stress is related to the global maximum, thus the two mechanisms should be compared to define the increase in strength of the alloys. The increase of shear strength by modulus and lattice

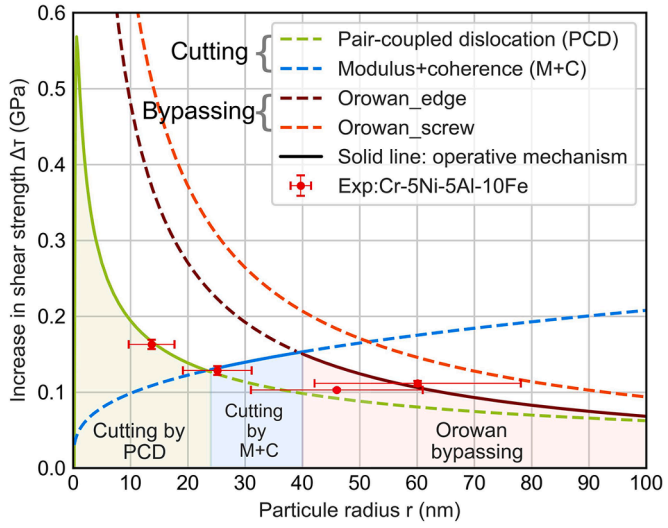

Fig. 13. The observed and calculated increase in shear stress for different precipitate strengthening mechanisms in Cr-5Ni-5Al-10Fe aged at 1000 °C. The red points from left to right represent the hardness as a function of the mean precipitate radius in samples aged for 4/20/100/240 h. The error bar shows the standard deviation of measured hardness and mean precipitate radius.

mismatch ($\Delta\tau_{m+c}$) is the sum of $\Delta\tau_{Coherency}$ and $\Delta\tau_{Modulus}$, calculated respectively using the following formula [99,103,111]:

$$\Delta\tau_{Modulus} = 0.0055\Delta G^{3/2}\left(\frac{\phi}{T}\right)^{\frac{1}{2}} b\left(\frac{r}{b}\right)^{\frac{3m}{2}-1} \times \left[0.94\left(1+2.5\eta_{SL}^{**}\right)^{\frac{1}{3}}\right] \quad (8)$$

where $\Delta G = G_{ppt} - G$ is the shear modulus difference between the precipitate and matrix phase with G_{ppt}=82.77 GPa [112] and G=105 GPa, $m = 0.85$ is a constant; and $\eta_{SL}^{**} = 1.09(\phi G/\Delta G)^{1/2}$ depends on the volume fraction an phase shear modulus.

$$\Delta\tau_{Coherency} = \alpha G\left(\frac{2|\delta|}{3}\right)^{\frac{3}{2}}\left(\frac{\phi r}{b}\right)^{\frac{1}{2}} \times \left[0.94\left(1+2.5\eta_{SL}^{*}\right)^{\frac{1}{3}}\right] \quad (9)$$

where α=4.1 is a constant [102], G=105 GPa, δ=0.162% is the measured lattice misfit by SXRD, and $\eta_{SL}^{*} = 0.54(3\phi b)^{0.5}(2|\delta|r)^{-0.5}$ for undissociated dislocations [104].

For the final operative mechanism, the Orowan bypassing can be activated when the Orowan stress becomes smaller than the shearing stress. The Orowan's stress is calculated using the following formula [105]:

$$\Delta\tau_{Or} = 0.9\frac{[ln(2\pi r/b)]^{3/2}}{[ln(L/b)]^{1/2}} \times \frac{K^{dipole}}{b\left[L-\left(\frac{\pi}{2}\right)r\right]} \quad (10)$$

where $L = r[2\pi/(3\phi)]^{0.5}$ is the interspacing of precipitates. The material related parameters are the same value used in Fe-superalloys which also have bcc structure [55]. K^{dipole} is a constant accounting for the statistical distribution in the glide plane and the elastic dipole interaction of the dislocation segments near the particles [113]. For an edge dislocation, $K_{edge} = \frac{Gb^2}{(2\pi)} = 1.041$ and, for a screw dislocation, $K_{screw} = \frac{Gb^2}{[2\pi(1-\nu)]} = 1.431$. All the parameters used are summarised in Table S2.

Fig. 13 presents the increase of shear strength due to the three mechanisms with dashed lines and the predicted active mechanism with the continuous line as a function of precipitate radius. It suggests that, at low particle radius (r < 24 nm), the low misfit and high anti-phase boundary energy (880 mJ/m^2 [93]) promote order strengthening via precipitate shearing by strong pair-coupled dislocation. This strengthening mechanism is believed to reduce strain accumulation at interfaces and prevent crack initiation [114]. For precipitates (24 < r < 40 nm), modulus and coherency strengthening dominate. The modulus and lattice mismatch strengthening is shown to be negligible in γ-γ' Ni-superalloys [99,111] but should be evaluated in Fe-superalloys [55,115]. For precipitates with a radius r > 40 nm, Orowan bypassing dominates over cutting. The increase in shear strength by experiment as a function of mean precipitate size shows a good agreement with the calculated contribution of three mechanisms. However, a large size distribution exists as represented by the horizontal error bars. When the ageing time is longer than 20 h, therefore could be simultaneous active mechanisms. It is interesting to note that the Orowan stress reduces slowly with the radius. Combined with the low coarsening rate of Cr (Fe)-NiAl, the quaternary alloy is expected to maintain its strength for a long operation period. Here, the mechanism analysis based on hardness predicts a transition of the main average mechanism, which requires onward validation. This type of analysis offers a guide as to the deformation mechanisms at play, and aids the further design optimisation of these first prototype alloys (*e.g.*, [115–117]).

5. Conclusions

In summary, this work has developed novel Cr-superalloys for high-temperature applications, where the A2-Cr(Fe) matrix is reinforced by nano-scale B2-NiAl precipitates. The following conclusions are drawn:

(1) Design of alloys using CALPHAD was paired with experiments. The microstructure of the ternary system and the one tailored by quaternary Fe additions were evaluated. The NiAl precipitate volume fraction can be increased with Fe alloying, owing to enhanced A2-solubility of Ni and Al due to the Fe additions. Experimentally measured phase compositions identify that the TCHEA6 database overestimates the solubility limit in the Cr-Ni-Al ternary alloys but is effective in predicting the increased solubility trend with quaternary Fe alloying.

(2) In both ternary Cr-Ni-Al and quaternary Cr-Ni-Al-Fe alloys, the creation of coherent B2-NiAl precipitates by ageing at 1000/1200 °C, after homogenisation in the A2-Cr(Fe) field (1400 °C) was experimentally demonstrated. A cube-to-cube $<100>_{A2}$//$<100>_{B2}$ orientation relationship with low lattice misfit ~ 0.1% between matrix and precipitates was identified.

(3) Cr-superalloys show diffusion-controlled coarsening behaviour with remarkably low coarsening rates (~10^2 nm^3/h at 1000 °C), compared to ferritic-superalloys (~10^8 nm^3/h), Co- and Ni-superalloys (~10^5 nm^3/h). These remarkable experimental values reflect the exceptional stability of the A2-B2 microstructure for high-temperature applications. Interface energies in Cr-superalloys are deduced to be ~40 mJ/m^2 at 1000 °C and ~20 mJ/m^2 at 1200 °C. The low coarsening rate is principally attributed to the low solubility of Ni and Al in the matrix.

(4) Cr-superalloys with Fe addition exhibit high strength from ~1300 MPa at room temperature to ~320 MPa at 1000 °C. While Fe moderately accelerates the coarsening kinetics, the quaternary alloys exhibit a high hardness of ~500 HV0.5, due to Fe solid solution strengthening as well as resistance to age-softening. Their strength is attributed to a combination of solid solution strengthening and precipitate strengthening. Different precipitate-strengthening mechanisms, from cutting to bypassing, operate with increasing precipitate size.

The strengthening mechanism analysis also provides new insights into the deformation behaviour of Cr-superalloys and possible pathways to control and enhance their mechanical properties. Further compositional tuning paired with thermomechanical processing could optimise the microstructure and grain structure for improved ductility. Future experiments will also investigate the creep/corrosion resistance and

thermal conductivity of Cr-Ni-Al-Fe alloys, with the aim to open up the novel material class of Cr-superalloys for high-temperature applications, such as advanced solar thermal and nuclear energy.

Disclaimer

The content of this publication reflects only the author's view and not necessary those of the European Commission. The Commission is not responsible for any use that may be made of the information this publication contains.

Declaration of Competing Interest

The authors declare that they have no known competing financial interests or personal relationships that could have appeared to influence the work reported in this paper.

Acknowledgement

This project has received funding from the European Union's Horizon 2020 research and innovation programme under grant agreement No 958418 "COMPASsCO2" (https://www.compassco2.eu). A Knowles acknowledges support from: UKRI Future Leaders Fellowship (MR/T019174/1) and Royal Academy of Engineering Research Fellowship (RF\201819\18\158). The atom probe facility at the University of Oxford is funded by EPSRC grant EP/T011505/1 and access was supported by UKRI-NNUF (Call 5 Application 58). The authors also acknowledge the Diamond Light Source (United Kingdom) for time on beamline I11 under proposal CY32708 and on instrument E02 in the electron Physical Science Imaging Centre (ePSIC) under proposal MG32309 supported by Dr Christopher Allen. The authors thank the Centre for Electron Microscopy (University of Birmingham) for their support & assistance in this work.

Supplementary materials

Supplementary material associated with this article can be found, in the online version, at doi:10.1016/j.actamat.2023.119183.

References

[1] S. Pfenninger, P. Gauché, J. Lilliestam, K. Damerau, F. Wagner, A. Patt, Potential for concentrating solar power to provide baseload and dispatchable power, Nat. Clim. Change. 4 (2014) 689–692, https://doi.org/10.1038/nclimate2276.
[2] C.K. Ho, M. Carlson, K.J. Albrecht, Z. Ma, S. Jeter, C.M. Nguyen, Evaluation of alternative designs for a high temperature particle-to-sCO2 heat exchanger, J. Sol. Energy Eng. 141 (2019).
[3] Y.-L. He, Y. Qiu, K. Wang, F. Yuan, W.-Q. Wang, M.-J. Li, J.-Q. Guo, Perspective of concentrating solar power, Energy 198 (2020), 117373.
[4] R.P. Merchán, M.J. Santos, A. Medina, A. Calvo Hernández, High temperature central tower plants for concentrated solar power: 2021 overview, Renew. Sustain. Energy Rev. 155 (2022), 111828, https://doi.org/10.1016/j.rser.2021.111828.
[5] H2020 EU project: COMPASsCO2., H2020 EU Proj. COMPASsCO2. (n.d.). https://www.compassco2.eu.
[6] Heliogen - First Quarter 2022 Presentation, 2022. https://heliogen.com.
[7] M. Sarvghad, S.D. Maher, D. Collard, M. Tassan, G. Will, T.A. Steinberg, Materials compatibility for the next generation of Concentrated Solar Power plants, Energy Storage Mater 14 (2018) 179–198.
[8] J. Yin, Q. Zheng, Z. Peng, X. Zhang, Review of supercritical CO2 power cycles integrated with CSP, Int. J. Energy Res. 44 (2020) 1337–1369.
[9] W.D. Klopp, Recent developments in chromium and chromium alloys, JOM 21 (1969) 23–32.
[10] A.T. Dinsdale, SGTE data for pure elements, Calphad 15 (1991) 317–425.
[11] C.T. Sims, The Case for Chromium: by-passed until now, What are the prospects for Cr-alloys in high-temperature service? JOM 15 (1963) 127–132.
[12] Y. Gu, H. Harada, Y. Ro, Chromium and chromium-based alloys: problems and possibilities for high-temperature service, Jom 56 (2004) 28–33.
[13] D. Maykuth, A. Gilbert, Chromium and Chromium alloys, Defense Metals Information Center, Battelle Memorial Institute, 1966.
[14] F.E. Block, P.C. Good, G. Asai, Electrodeposition of High-Purity Chromium, J. Electrochem. Soc. 106 (1959) 43.
[15] R. Hook, A. Adair, H. Lipsitt, Observations on the ductility and fracture of recrystallized chromium, Trans. Metall. Soc. AIME 221 (1961) 409–411.
[16] Y. Matsumoto, K. Oki, M. Tanaka, F. Fujigami, Y. Harada, M. Morinaga, Room-temperature ductility and surface notch sensitivity of chromium alloyed with vanadium and molybdenum, Mater. Sci. Eng. A. 385 (2004) 133–139, https://doi.org/10.1016/j.msea.2004.05.086.
[17] C. Reid, A. Gilbert, Dislocation structure in chromium, chromium-rhenium, and chromium-iron alloys, J. Common Met. 10 (1966) 77–90.
[18] J.R. Stephens, W.R. Witzke, Alloy softening in group VIA metals alloyed with rhenium, J. Common Met. 23 (1971) 325–342.
[19] C. Wukusick, Rhenium Ductilizing Effect. General Electric Nuclear Materials and Propulsion Operation, 1967. Evendale, Ohio.
[20] J.R. Stephens, W.D. Klopp, Ductility Mechanisms and Superplasticity in Chromium Alloys, National Aeronautics and Space Administration, 1968.
[21] W.D. Klopp, A review of chromium, molybdenum, and tungsten alloys, J. Common Met. 42 (1975) 261–278.
[22] A.S. Dorcheh, M.C. Galetz, Challenges in developing oxidation-resistant chromium-based alloys for applications above 900° C, Jom 68 (2016) 2793–2802.
[23] R.C. Reed, The superalloys: Fundamentals and Applications, Cambridge university press, 2008.
[24] H. Calderon, M. Fine, J. Weertman, Coarsening and morphology of β′ particles in Fe-Ni-Al-Mo ferritic alloys, Metall. Trans. A. 19 (1988) 1135–1146.
[25] C. Stallybrass, G. Sauthoff, Ferritic Fe–Al–Ni–Cr alloys with coherent precipitates for high-temperature applications, Mater. Sci. Eng. A. 387 (2004) 985–990.
[26] L. Royer, S. Mathieu, C. Liebaut, P. Steinmetz, Study of the microstructure and oxidation behavior of chromium base alloys strengthened by NiAl precipitates. Trans Tech Publ, 2008, pp. 117–125.
[27] Ö. Doğan, X. Song, D. Palacio, M. Gao, Coherent precipitation in a high-temperature Cr–Ni–Al–Ti Alloy, J. Mater. Sci. 49 (2014) 805–810.
[28] D. Locq, P. Caron, C. Ramusat, R. Mévrel, Quaternary chromium-based alloys strengthened by Heusler phase precipitation, Mater. Sci. Eng. A. 647 (2015) 322–332, https://doi.org/10.1016/j.msea.2015.09.033.
[29] A.J. Knowles, D. Dye, R.J. Dodds, A. Watson, C.D. Hardie, S.A. Humphry-Baker, Tungsten-based bcc-superalloys, Appl. Mater. Today. 23 (2021), 101014, https://doi.org/10.1016/j.apmt.2021.101014.
[30] A.J. Knowles, T.-S. Jun, A. Bhowmik, N.G. Jones, T.B. Britton, F. Giuliani, H. J. Stone, D. Dye, A new beta titanium alloy system reinforced with superlattice intermetallic precipitates, Scr. Mater 140 (2017) 71–75, https://doi.org/10.1016/j.scriptamat.2017.06.038.
[31] B.D. Cullity, Elements of X-ray Diffraction, Addison-Wesley Publishing, 1956.
[32] T. Hughes, E. Lautenschlager, J. Cohen, J. Brittain, X-Ray Diffraction Investigation of β′-NiAl Alloys, J. Appl. Phys. 42 (1971) 3705–3716.
[33] S. Huang, Y. Gao, K. An, L. Zheng, W. Wu, Z. Teng, P.K. Liaw, Deformation mechanisms in a precipitation-strengthened ferritic superalloy revealed by *in situ* neutron diffraction studies at elevated temperatures, Acta Mater 83 (2015) 137–148.
[34] S.-I. Baik, M.J.S. Rawlings, D.C. Dunand, Effect of hafnium micro-addition on precipitate microstructure and creep properties of a Fe-Ni-Al-Cr-Ti ferritic superalloy, Acta Mater 153 (2018) 126–135, https://doi.org/10.1016/j.actamat.2018.04.044.
[35] V. Soni, B. Gwalani, T. Alam, S. Dasari, Y. Zheng, O.N. Senkov, D. Miracle, R. Banerjee, Phase inversion in a two-phase, BCC+ B2, refractory high entropy alloy, Acta Mater 185 (2020) 89–97.
[36] C. Zhang, H. Wang, X. Wang, Y.T. Tang, Q. Yu, C. Zhu, M. Xu, S. Zhao, R. Kou, X. Wang, B.E. MacDonald, R.C. Reed, K.S. Vecchio, P. Cao, T.J. Rupert, E. J. Lavernia, Strong and ductile refractory high-entropy alloys with super formability, Acta Mater 245 (2023), 118602, https://doi.org/10.1016/j.actamat.2022.118602.
[37] P. Kumar, S.J. Kim, Q. Yu, J. Ell, M. Zhang, Y. Yang, J.Y. Kim, H.-K. Park, A. M. Minor, E.S. Park, Compressive *vs.* tensile yield and fracture toughness behavior of a body-centered cubic refractory high-entropy superalloy Al0. 5Nb1. 25Ta1. 25TiZr at temperatures from ambient to 1200° C, Acta Mater 245 (2023), 118620.
[38] N. Dupin, I. Ansara, B. Sundman, Thermodynamic re-assessment of the ternary system Al-Cr-Ni, Calphad 25 (2001) 279–298.
[39] S. Han, D. Young, Simultaneous internal oxidation and nitridation of Ni–Cr–Al alloys, Oxid. Met. 55 (2001) 223–242.
[40] Y. Wang, G. Cacciamani, Thermodynamic modeling of the Al-Cr-Ni system over the entire composition and temperature range, J. Alloys Compd. 688 (2016) 422–435.
[41] I. Kornilov, R. Mints, The Fusibility Diagram of the Ni-Cr-NiAl System, 1954, pp. 1085–1088.
[42] Y.A. Bagaryatskiy, The Cr corner of the Cr-Ni-Al system and the Cr-NiAl pseudobinary section, Zh Neorg Khim 3 (1958) 722–728.
[43] G. Song, Z. Sun, L. Li, B. Clausen, S.Y. Zhang, Y. Gao, P.K. Liaw, High temperature deformation mechanism in hierarchical and single precipitate strengthened ferritic alloys by *in situ* neutron diffraction studies, Sci. Rep. 7 (2017) 1–14.
[44] A. Ma, D. Dye, R. Reed, A model for the creep deformation behaviour of single-crystal superalloy CMSX-4, Acta Mater 56 (2008) 1657–1670.
[45] I. Arganda-Carreras, V. Kaynig, C. Rueden, K.W. Eliceiri, J. Schindelin, A. Cardona, H.Sebastian Seung, Trainable Weka Segmentation: a machine learning tool for microscopy pixel classification, Bioinformatics 33 (2017) 2424–2426, https://doi.org/10.1093/bioinformatics/btx180.
[46] Z. Xia, K. Ma, S. Cheng, T. Blackburn, Z. Peng, K. Zhu, W. Zhang, D. Xiao, A. J. Knowles, R. Arcucci, Accurate identification and measurement of the

precipitate area by two-stage deep neural networks in novel chromium-based alloys, Phys. Chem. Chem. Phys. 25 (2023) 15970–15987, https://doi.org/10.1039/D3CP00402C.
[47] E. Nembach, E. Nembach, Particle Strengthening of Metals and Alloys, Wiley, New York, 1997.
[48] Z. Sun, G. Song, J. Ilavsky, G. Ghosh, P.K. Liaw, Nano-sized precipitate stability and its controlling factors in a NiAl-strengthened ferritic alloy, Sci. Rep. 5 (2015) 16081, https://doi.org/10.1038/srep16081.
[49] M. Aizenshtein, E. Strumza, E. Brosh, S. Hayun, Precipitation kinetics, microstructure, and equilibrium state of A2 and B2 phases in multicomponent Al2.75CoCrFeNi alloy, J. Mater. Sci. 55 (2020) 7016–7028, https://doi.org/10.1007/s10853-020-04487-9.
[50] I.M. Lifshitz, V.V. Slyozov, The kinetics of precipitation from supersaturated solid solutions, J. Phys. Chem. Solids. 19 (1961) 35–50.
[51] C. Wagner, Theorie der alterung von niederschlägen durch umlösen (Ostwald-reifung), Z. Für Elektrochem. Berichte Bunsenges, Für Phys. Chem 65 (1961) 581–591.
[52] G. Kostorz, Phase Transformations in Materials, Wiley Online Library, 2001.
[53] H.J. Rosales-Dorantes, N. Cayetano-Castro, V.M. Lopez-Hirata, M.L. Saucedo-Muñoz, D. Villegas-Cardenas, F. Hernández-Santiago, Coarsening process of coherent β' precipitates in Fe–10wt-%Ni–15wt-%Al and Fe–10wt-%Ni–15wt-%Al–1wt-%Cu alloys, Mater. Sci. Technol. 29 (2013) 1492–1498, https://doi.org/10.1179/1743284713Y.0000000315.
[54] P.A. Ferreirós, P.R. Alonso, G.H. Rubiolo, Coarsening process and precipitation hardening in Fe2AlV-strengthened ferritic Fe76Al12V12 alloy, Mater. Sci. Eng. A. 684 (2017) 394–405.
[55] P.A. Ferreirós, P. Alonso, G.H. Rubiolo, Effect of Ti additions on phase transitions, lattice misfit, coarsening, and hardening mechanisms in a Fe2AlV-strengthened ferritic alloy, J. Alloys Compd. 806 (2019) 683–697.
[56] S. Meher, S. Nag, J. Tiley, A. Goel, R. Banerjee, Coarsening kinetics of γ′ precipitates in cobalt-base alloys, Acta Mater 61 (2013) 4266–4276, https://doi.org/10.1016/j.actamat.2013.03.052.
[57] D.J. Sauza, D.C. Dunand, D.N. Seidman, Microstructural evolution and high-temperature strength of a γ(f.c.c.)/γ'(L12) Co–Al–W–Ti–B superalloy, Acta Mater 174 (2019) 427–438, https://doi.org/10.1016/j.actamat.2019.05.058.
[58] A.M. Ges, O. Fornaro, H.A. Palacio, Coarsening behaviour of a Ni-base superalloy under different heat treatment conditions, Mater. Sci. Eng. A. 458 (2007) 96–100, https://doi.org/10.1016/j.msea.2006.12.107.
[59] S. Zhao, X. Xie, G.D. Smith, S.J. Patel, Gamma prime coarsening and age-hardening behaviors in a new nickel base superalloy, Mater. Lett. 58 (2004) 1784–1787, https://doi.org/10.1016/j.matlet.2003.10.053.
[60] K. Kusabiraki, X. Zhang, T. Ooka, The Growth of γ'Precipitates in a 53Ni-20Co-15Cr Superalloy, ISIJ Int 35 (1995) 1115–1120.
[61] M.R. Jahangiri, H. Arabi, S.M.A. Boutorabi, Comparison of microstructural stability of IN939 superalloy with two different manufacturing routes during long-time aging, Trans. Nonferrous Met. Soc. China. 24 (2014) 1717–1729, https://doi.org/10.1016/S1003-6326(14)63245-3.
[62] J. Zhang, L. Liu, T. Huang, J. Chen, K. Cao, X. Liu, J. Zhang, H. Fu, Coarsening kinetics of γ′ precipitates in a *Re*-containing Ni-based single crystal superalloy during long-term aging, J. Mater. Sci. Technol. 62 (2021) 1–10, https://doi.org/10.1016/j.jmst.2020.05.034.
[63] W. Huang, Y.A. Chang, Thermodynamic properties of the Ni–Al–Cr system, Intermetallics 7 (1999) 863–874, https://doi.org/10.1016/S0966-9795(98)00138-1.
[64] W. Cao, J. Zhu, Y. Yang, F. Zhang, S. Chen, W.A. Oates, Y.A. Chang, Application of the cluster/site approximation to fcc phases in Ni–Al–Cr system, Acta Mater 53 (2005) 4189–4197, https://doi.org/10.1016/j.actamat.2005.05.016.
[65] B. Tang, D.A. Cogswell, G. Xu, S. Milenkovic, Y. Cui, The formation mechanism of eutectic microstructures in NiAl–Cr composites, Phys. Chem. Chem. Phys. 18 (2016) 19773–19786.
[66] C. Mathiou, K. Giorspyros, E. Georgatis, A. Karantzalis, Microstructural verification of the theoretically predicted morphologies of the NiAl–Cr pseudo-binary alloy systems and NiAl–Cr eutectic structure modification by Mo addition, SN Appl. Sci. 1 (2019) 1–10.
[67] J. Tiley, G. Viswanathan, R. Srinivasan, R. Banerjee, D. Dimiduk, H. Fraser, Coarsening kinetics of γ′ precipitates in the commercial nickel base Superalloy René 88 DT, Acta Mater 57 (2009) 2538–2549.
[68] W. Liu, J. Li, W. Zheng, Q. Jiang, Ni Al, (110)/ Cr (110) interface: a density functional theory study, Phys. Rev. B. 73 (2006), 205421.
[69] T. Philippe, P.W. Voorhees, Ostwald ripening in multicomponent alloys, Acta Mater 61 (2013) 4237–4244, https://doi.org/10.1016/j.actamat.2013.03.049.
[70] C. Marsh, H. Chen, An *in situ* x-ray diffraction study of precipitation from a supersaturated solid solution: the γ′ precipitate in a Ni-12.5 at.% A1 alloy, Acta Metall. Mater. 38 (1990) 2287–2298.
[71] S.Q. Xiao, P.-J. Wilbrandt, P. Haasen, HREM observation of the nucleation of γ′-precipitates at dislocations in a Ni-12at%Al alloy, Scr. Metall. 23 (1989) 295–300, https://doi.org/10.1016/0036-9748(89)90370-0.
[72] A. Azzam, T. Philippe, A. Hauet, F. Danoix, D. Locq, P. Caron, D. Blavette, Kinetics pathway of precipitation in model Co-Al-W superalloy, Acta Mater 145 (2018) 377–387, https://doi.org/10.1016/j.actamat.2017.12.032.
[73] K. Delargy, Phase composition and phase stability of a high-chromium nickel-based superalloy, IN939, Metall. Trans. A. 14 (1983) 1771–1783.
[74] H. Wu, T. Mayeshiba, D. Morgan, High-throughput ab-initio dilute solute diffusion database, Sci. Data. 3 (2016), 160054, https://doi.org/10.1038/sdata.2016.54.
[75] S. Neumeier, H.U. Rehman, J. Neuner, C.H. Zenk, S. Michel, S. Schuwalow, J. Rogal, R. Drautz, M. Göken, Diffusion of solutes in fcc Cobalt investigated by diffusion couples and first principles kinetic Monte Carlo, Acta Mater 106 (2016) 304–312, https://doi.org/10.1016/j.actamat.2016.01.028.
[76] A. Bezold, N. Volz, M. Lenz, N. Karpstein, C. Zenk, E. Spiecker, M. Göken, S. Neumeier, Quantification of the temperature-dependent evolution of defect structures in a CoNi-base superalloy, Acta Mater 227 (2022), 117702.
[77] M. Kolb, L.P. Freund, F. Fischer, I. Povstugar, S.K. Makineni, B. Gault, D. Raabe, J. Müller, E. Spiecker, S. Neumeier, On the grain boundary strengthening effect of boron in γ/γ′ Cobalt-base superalloys, Acta Mater 145 (2018) 247–254.
[78] Y. Chen, C. Wang, J. Ruan, T. Omori, R. Kainuma, K. Ishida, X. Liu, High-strength Co–Al–V-base superalloys strengthened by γ′-Co3 (Al, V) with high solvus temperature, Acta Mater 170 (2019) 62–74.
[79] P. Pandey, A.K. Sawant, B. Nithin, Z. Peng, S.K. Makineni, B. Gault, K. Chattopadhyay, On the effect of *Re* addition on microstructural evolution of a CoNi-based superalloy, Acta Mater 168 (2019) 37–51.
[80] J.R. Davis, Nickel, cobalt, and Their Alloys, ASM international, 2000.
[81] A. Suzuki, G.C. DeNolf, T.M. Pollock, Flow stress anomalies in γ/γ′ two-phase Co–Al–W-base alloys, Scr. Mater. 56 (2007) 385–388, https://doi.org/10.1016/j.scriptamat.2006.10.039.
[82] C. Stallybrass, G. Sauthoff, Ferritic Fe–Al–Ni–Cr alloys with coherent precipitates for high-temperature applications, in: 13th Int. Conf. Strength Mater 387–389, 2004, pp. 985–990, https://doi.org/10.1016/j.msea.2004.01.108.
[83] D.L. Harrod, R.E. Gold, Mechanical properties of vanadium and vanadium-base alloys, Int. Met. Rev. 25 (1980) 163–222, https://doi.org/10.1179/imtr.1980.25.1.163.
[84] N.E. Prasad, R.J. Wanhill, Aerospace Materials and Material Technologies, Springer, 2017.
[85] S.V. Raj, A preliminary assessment of the properties of a chromium silicide alloy for aerospace applications, in: 3rd Int. Conf. High Temp. Intermet 192–193, 1995, pp. 583–589, https://doi.org/10.1016/0921-5093(94)03281-5.
[86] P.A. Ferreirós, P.R. Alonso, G.R. Gomez, G.H. Rubiolo, Impact toughness transition temperature of ferritic Fe-Al-V alloy with strengthening Fe2AlV precipitates, Mater. Sci. Eng. A. 706 (2017) 136–141, https://doi.org/10.1016/j.msea.2017.09.001.
[87] R. Krein, M. Friak, J. Neugebauer, M. Palm, M. Heilmaier, L21-ordered Fe–Al–Ti alloys, Intermetallics 18 (2010) 1360–1364.
[88] A. Michalcová, L. Senčekova, G. Rolink, A. Weisheit, J. Pešička, M. Stobik, M. Palm, Laser additive manufacturing of iron aluminides strengthened by ordering, borides or coherent Heusler phase, Mater. Des. 116 (2017) 481–494.
[89] P. Ferreirós, U. Sterin, P. Alonso, A. Knowles, G. Rubiolo, Influence of precipitate and grain sizes on the brittle-to-ductile transition in Fe–Al–V bcc-L21 ferritic superalloys, Mater. Sci. Eng. A. 856 (2022), 144031.
[90] Y.F. Gu, Y. Ro, H. Harada, Tensile properties of chromium alloyed with silver, Metall. Mater. Trans. A. 35 (2004) 3329–3331, https://doi.org/10.1007/s11661-006-0237-1.
[91] M.C. Gao, Ö.N. Doğan, P. King, A.D. Rollett, M. Widom, The first-principles design of ductile refractory alloys, Jom 60 (2008) 61–65.
[92] T. Hong, A.J. Freeman, Effect of antiphase boundaries on the electronic structure and bonding character of intermetallic systems: niAl, Phys. Rev. B. 43 (1991) 6446–6458, https://doi.org/10.1103/PhysRevB.43.6446.
[93] A. Sengupta, S. Putatunda, L. Bartosiewicz, J. Hangas, P. Nailos, M. Peputapeck, F. Alberts, Tensile behavior of a new single-crystal nickel-based superalloy (CMSX-4) at room and elevated temperatures, J. Mater. Eng. Perform. 3 (1994) 73–81.
[94] D. Tabor, Indentation hardness: fifty years on a personal view, Philos. Mag. A. 74 (1996) 1207–1212.
[95] J. Rosenberg, H. Piehler, Calculation of the Taylor factor and lattice rotations for bcc metals deforming by pencil glide, Metall. Trans. 2 (1971) 257–259.
[96] E. Nembach, G. Neite, Precipitation hardening of superalloys by ordered γ′-particles, Prog. Mater. Sci. 29 (1985) 177–319.
[97] A.J. Ardell, Yielding in, Crystals Containing Finite Dispersed Obstacles, in: K.H. J. Buschow, R.W. Cahn, M.C. Flemings, B. Ilschner, E.J. Kramer, S. Mahajan, P. Veyssière (Eds.), Encycl. Mater. Sci. Technol., Elsevier, Oxford, 2001, pp. 9842–9854, https://doi.org/10.1016/B0-08-043152-6/01782-4.
[98] A.J. Ardell, Precipitation hardening, Metall. Trans. A. 16 (1985) 2131–2165.
[99] R. Schwarz, R. Labusch, Dynamic simulation of solution hardening, J. Appl. Phys. 49 (1978) 5174–5187.
[100] B. Reppich, P. Schepp, G. Wehner, Some new aspects concerning particle hardening mechanisms in γ'precipitating nickel-base alloys—II, Experiments, Acta Metall 30 (1982) 95–104.
[101] B. Reppich, On the attractive particle–dislocation interaction in dispersion-strengthened material, Acta Mater 46 (1998) 61–67.
[102] L. Brown, R. Ham, Dislocation-particle interactions, Strength. Methods Cryst. (1971) 9–135.
[103] E. Nembach, Hardening by coherent precipitates having a lattice mismatch: the effect of dislocation splitting, Scr. Metall. 18 (1984) 105–110.
[104] U. Kocks, Theory of an obstacle-controlled yield strength: report after an international workshop, Mater Sci Eng Netherlands 27 (1977).
[105] M.F. Ashby, The theory of the critical shear stress and work hardening in dispersion-hardened crystals. Harvard Univ Cambridge Mass Div of Engineering and Applied Physics, 1966.
[106] W. Hüther, B. Reppich, Order hardening of MgO by large precipitated volume fractions of spinel particles, Mater. Sci. Eng. 39 (1979) 247–259, https://doi.org/10.1016/0025-5416(79)90063-6.

[107] J. Lenkkeri, The elastic moduli of some body-centred cubic titanium-vanadium, vanadium-chromium and chromium-iron alloys, J. Phys. F Met. Phys. 10 (1980) 611.
[108] C.L. Fu, M. Yoo, Deformation behavior of B2 type aluminides: feAl and NiAl, Acta Metall. Mater. 40 (1992) 703–711.
[109] P. Veyssiere, R. Noebe, Weak-beam study of< 111>superlattice dislocations in NiAl, Philos. Mag. A. 65 (1992) 1–13.
[110] B. Reppich, Particle strengthening, Mater. Sci. Technol. (2006).
[111] C. Hu, Z. Zhang, H. Chen, J. He, H. Guo, Reactive elements dependence of elastic properties and stacking fault energies of γ-Ni, γ′-Ni3Al and β-NiAl, J. Alloys Compd. 843 (2020), 155799, https://doi.org/10.1016/j.jallcom.2020.155799.
[112] M.F. Ashby, Results and consequences of a recalculation of the frank-read and the orowan stress, Acta Metall 14 (1966) 679–681, https://doi.org/10.1016/0001-6160(66)90074-5.
[113] S. Jiang, H. Wang, Y. Wu, X. Liu, H. Chen, M. Yao, B. Gault, D. Ponge, D. Raabe, A. Hirata, Ultrastrong steel via minimal lattice misfit and high-density nanoprecipitation, Nature 544 (2017) 460–464.
[114] Z. Jiao, J. Luan, M. Miller, C. Yu, Y. Liu, C. Liu, Precipitate transformation from NiAl-type to Ni2AlMn-type and its influence on the mechanical properties of high-strength steels, Acta Mater 110 (2016) 31–43.
[115] L. Zhang, Y. Wen, Y. Liu, F. Quan, J. Han, S. Yang, X. Chen, S. He, O.I. Gorbatov, X. Chen, Cr-promoted formation of B2+ L21 composite nanoprecipitates and enhanced mechanical properties in ferritic alloy, Acta Mater 243 (2023), 118506.
[116] N.Q. Vo, D.C. Dunand, D.N. Seidman, Role of silicon in the precipitation kinetics of dilute Al-Sc-Er-Zr alloys, Mater. Sci. Eng. A. 677 (2016) 485–495.
[117] D. Collins, H. Stone, A modelling approach to yield strength optimisation in a nickel-base superalloy, Int. J. Plast. 54 (2014) 96–112.